ELSEVIER

Journal of Structural Geology 27 (2005) 1315–1343

JOURNAL OF STRUCTURAL GEOLOGY

www.elsevier.com/locate/jsg

Strain patterns within part of the Willard thrust sheet, Idaho–Utah–Wyoming thrust belt

Adolph Yonkee

Department of Geosciences, Weber State University, Ogden, UT 84408-2507, USA

Received 1 July 2003; received in revised form 10 March 2004; accepted 24 June 2004
Available online 14 October 2004

Abstract

The Willard thrust sheet, located in northern Utah, USA, contains a 10–15-km-thick sequence of strata that were internally deformed and translated about 50 km ESE. Upper levels of the sheet are relatively little deformed, lower levels have minor folds and cleavage that increase in intensity downward and rotate into parallelism with the thrust, and the basal fault zone contains mylonite and ultracataclasite. Finite strain displays systematic changes with structural position and lithology. Basal levels have strain ratios ($R \approx R_{XZ}$) of 3–5, and angles (θ) between stretch directions and the thrust of $<10°$ in the profile plane. Diamictite, slate, and greywacke at lower levels have R of 1.5–3 and θ of 10–35°, with overall correlations between increasing R, decreasing θ, and greater mica content. Overlying micaceous quartzite has relatively low strain, with R of 1.3–2 and $\theta > 50°$. Principal stretching (X) directions trend perpendicular to oblique to minor fold axes, which are locally oblique to the overall transport direction, reflecting partial decoupling of internal deformation from thrust slip. Principal axial ratios have $R_{YZ} > R_{XY}$, but microfabrics indicate only limited extension in the intermediate stretching direction (Y), corresponding to volume losses of about 10–40%. Strain is factored into components of thrust-perpendicular thinning and thrust-parallel shear that increase downward and in mica-rich layers, minor thrust-parallel shortening to extension, minor longitudinal extension, and minor longitudinal (wrench) shear. These patterns reflect litho-mechanical layering of the thrust sheet, which includes a very weak basal fault zone that formed at elevated fluid pressures, a weak mica-rich lower level with widespread crystal plastic and mass transfer deformation, and a stronger upper part with limited internal deformation.
© 2004 Elsevier Ltd. All rights reserved.

Keywords: Strain; Fold-thrust belt; Microtextures; Vorticity

1. Introduction

Although the large-scale geometry of many fold–thrust belts is relatively well known and consistent (e.g. Boyer and Elliot, 1982), characteristics of internal deformation are generally less well understood and more variable (e.g. Sanderson, 1982). Within fold–thrust belts, the total displacement field includes bulk translation on major faults, bulk rotation from large-scale folds, and internal deformation from grain-scale strain, cleavage, minor folds, and minor fault and vein arrays. Internal deformation may constitute a significant component of the total displacement field, and must be understood for estimating total shortening, reconstructing wedge taper, and calculating mass and energy balances (Mitra, 1994). Patterns of internal deformation vary between thrust sheets and may be partly decoupled from bulk translation. For example, the Morcles thrust sheet has a bulk translation <15 km, but displays extensive internal deformation (Ramsay et al., 1983), whereas the Lewis thrust sheet has a bulk translation >35 km, but displays only limited internal deformation (Mitra and Boyer, 1999). Such different patterns may reflect varying material properties of fault zones and thrust sheets, environmental factors (such as temperature and fluid pressure), and complex boundary conditions. In order to understand processes responsible for evolution of fold–thrust belts, characteristics of internal deformation, including strain patterns, must first be evaluated.

Idealized, two-dimensional kinematic models of internal deformation in thrust sheets include components of thrust-parallel simple shear that increases toward the base of the

E-mail address: ayonkee@weber.edu.

0191-8141/$ - see front matter © 2004 Elsevier Ltd. All rights reserved.
doi:10.1016/j.jsg.2004.06.014

sheet, and pure shear involving thrust-parallel (horizontal) shortening or extension in the transport direction, and thrust-perpendicular (vertical) thickening or thinning (Fig. 1A–C) (Sanderson, 1982). Simple shear may be associated with heterogeneous flow in a viscous boundary layer near the thrust, and pure shear may reflect thickening or thinning needed to maintain wedge taper (Mitra, 1994). Volume loss is also significant in some thrust sheets, such that vertical thinning may occur without significant thrust-parallel extension (Ring et al., 2001). Three-dimensional models include additional components of longitudinal shortening or extension perpendicular to the transport direction, and longitudinal (wrench) shear (Fig. 1D). These additional components may be related to varying translation magnitudes and directions within thrust sheets around salients (Hindle and Burkhard, 1999).

Natural thrust sheets display varying patterns of internal deformation partly described by these models. For example, strain patterns for quartzite in the Moine thrust zone record widespread thrust-parallel shortening and simple shear (Coward and Kim, 1981), and patterns for greywacke in the Glarus thrust sheet record significant thrust-perpendicular thinning and minor simple shear (Ring et al., 2001). Thus, many thrust sheets have undergone internal deformation involving general sub-simple shear (Simpson and De Paor, 1993). Some thrust sheets also display three-dimensional complications that record varying longitudinal shortening to extension, longitudinal (wrench) shear, and thrust-tip strain (Hossack, 1968; Coward and Potts, 1983).

Recent strain studies in the Idaho–Utah–Wyoming thrust belt of the North American Cordillera also reveal interesting patterns. Reconnaissance studies of frontal thrust sheets indicate relatively simple patterns with heterogeneous simple shear concentrated in weaker layers and near thrusts, and minor thrust-parallel shortening that increases westward toward the internal part of the belt (Mitra, 1994). Detailed strain studies of quartz-rich lithologies in the internal Sheep Rock thrust sheet in central Utah reveal more complex strain patterns with spatially variable simple shear, thrust-parallel extension to shortening, and longitudinal extension (Mukul and Mitra, 1998). Initial strain studies of the internal Willard sheet in northern Utah also reveal complex patterns (Yonkee, 1997), which are more extensively explored in this paper.

Characteristics of internal deformation in fold–thrust belts raise several questions. (1) What are the relative contributions of heterogeneous simple shear, thrust-parallel shortening, thrust-perpendicular thinning, and volume loss in thrust sheets? (2) Is plane strain a valid approximation or do strain patterns generally have three-dimensional complexities? (3) How are patterns of internal deformation related to structural position, lithology, and deformation conditions? In order to partly answer these questions, results of detailed structural and strain analysis for part of the

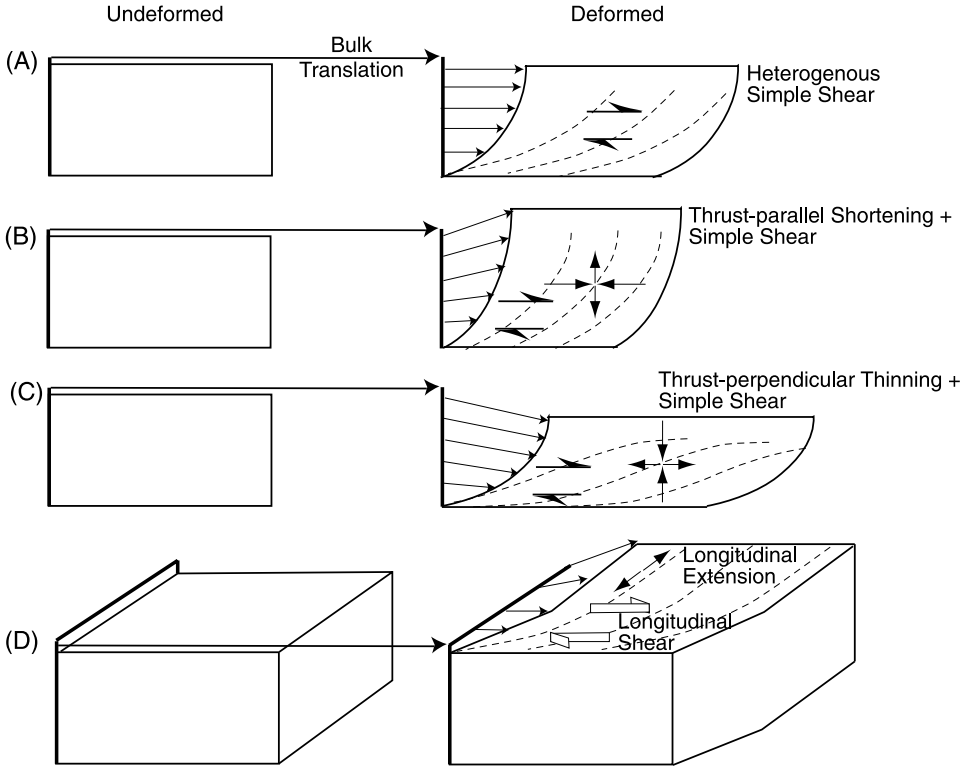

Fig. 1. Idealized models of internal deformation in thrust sheets related to: (A) heterogeneous simple shear that increases toward base of the sheet; (B) combined thrust-parallel shortening and simple shear; (C) combined thrust-perpendicular thinning and simple shear; and (D) three-dimensional components of longitudinal (wrench) shear and longitudinal extension perpendicular to the bulk translation direction (long arrow). General cleavage trajectories indicated by dashed lines. Internal deformation adds displacement components (small arrows) in thrust sheets. Modified from Sanderson (1982).

Willard thrust sheet are described and used to develop a kinematic model for internal deformation of this aerially extensive and far-traveled sheet.

2. Geologic setting

The Idaho–Utah–Wyoming belt is characterized by folds and thrusts that shortened and translated strata eastward toward the craton during the Early Cretaceous to Early Tertiary (Royse, 1993). The belt is divided into: (1) a western thrust system, including the Willard, Paris, and Meade thrusts, which carries a thicker sequence of Neoproterozoic to Paleozoic miogeoclinal strata that were deformed during the Early Cretaceous; and (2) an eastern thrust system, including the Crawford, Absaroka, and Hogsback thrusts, which carries a thinner sequence of Paleozoic strata that were deformed during the Late Cretaceous to early Eocene (Fig. 2A) (Coogan, 1992). The basement-cored Wasatch anticlinorium formed synchronously with the eastern system (Yonkee, 1992), and uplifted and tilted parts of the Willard thrust sheet.

Regional structural trends in the western thrust system define a broad salient convex to the east, curving from overall NNE-trending in the southern part, to NW-trending in the northern part (Fig. 2A). The Willard thrust in the southern part of the system has about 50 km of top-to-ESE slip based on regional cutoff relations (Yonkee, 1997). The Paris and Meade thrusts in the central part of the system, respectively, have about 20 and 40 km of top-to-E slip (DeCelles et al., 1993; Royse, 1993).

The western thrust system had a protracted deformation history based on relations of synorogenic deposits (DeCelles et al., 1993). The Neocomian to Aptian (130–115 Ma) lower Gannett Group records early slip on the Willard and Paris thrusts, the Aptian to Albian (115–100 Ma) upper Gannett Group records major slip on the Willard and Meade thrusts, and Cenomanian to Turonian (100–90 Ma) strata may record late slip on the system. $^{40}Ar/^{39}Ar$ ages of muscovite from syntectonic veins in the base of the Willard sheet vary mostly from 140 to 110 Ma, recording internal deformation that overlapped with major thrust slip (Yonkee et al., 1989).

The lower part of the Willard thrust sheet underwent regional greenschist-facies metamorphism, with fluid

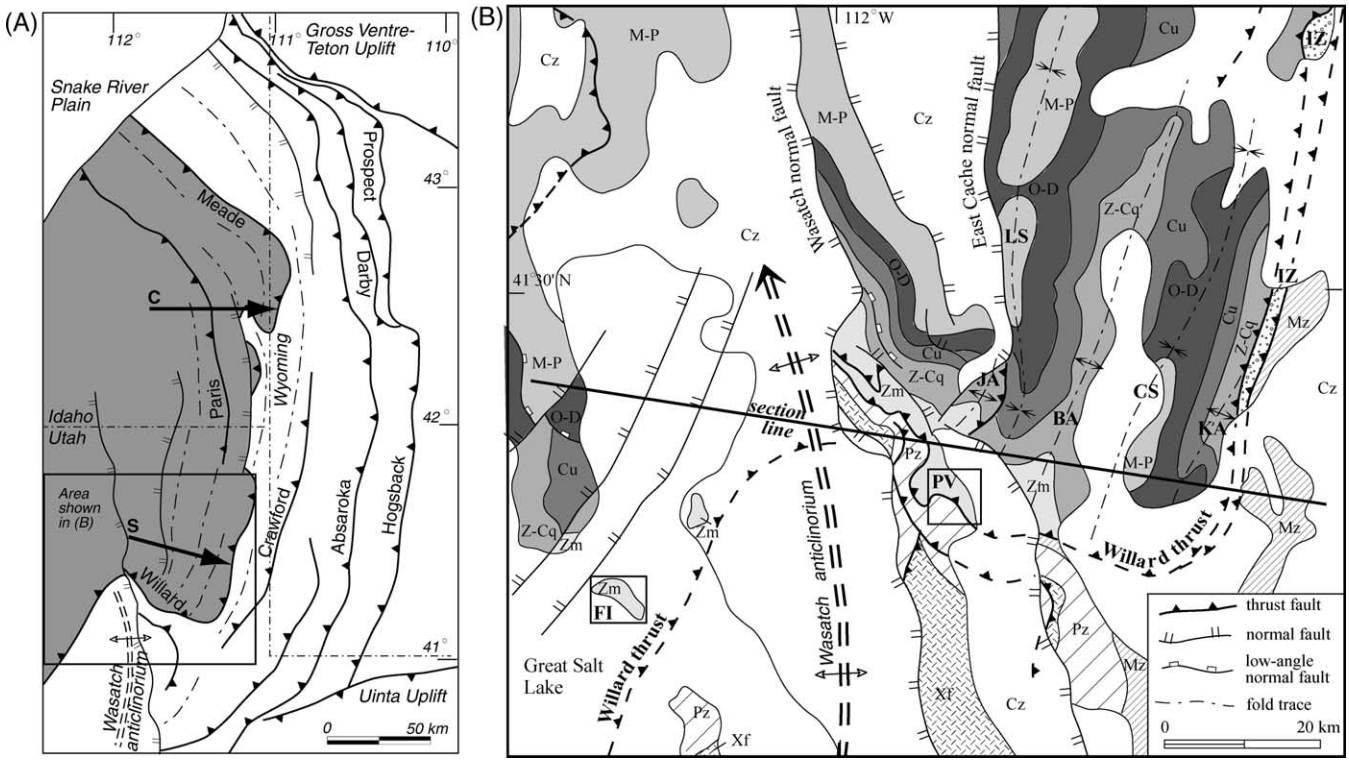

Fig. 2. (A) Index map of the Idaho–Utah–Wyoming thrust belt. Major thrust faults, foreland uplifts, and Wasatch anticlinorium labeled. The western thrust system, including the Willard, Paris, and Meade thrusts, carries thick miogeoclinal strata (shown in gray). Fold trends, indicated with dashed lines, and thrust traces define a salient convex to the east. General estimates of displacement direction and magnitude for the central (C) and southern (S) parts of the western thrust system indicated by large arrows (Royse, 1993; Yonkee, 1997). (B) Generalized geologic map of southern Willard thrust sheet. Major faults and crest of Wasatch anticlinorium indicated. Major folds are JA—James Peak anticline, LS—Logan Peak syncline, BA—Browns Hole anticline, CS—Causey syncline, KA—Knighton anticline, and IZ—imbricated zone that represents forelimb of fault propagation fold. Units in Willard sheet are Zm—Neoproterozoic micaceous strata, Z–Cq—upper Neoproterozoic to lower Cambrian quartz-rich strata, Cu—Cambrian carbonate-rich strata, O–D—Ordovician to Devonian strata, and M–P—Mississippian to Permian strata. Units in Willard footwall are Xf—Paleoproterozoic basement rocks of the Farmington Canyon Complex, Pz—Paleozoic strata, and Mz—Mesozoic strata. Cz—Cenozoic deposits. Study areas are FI—Fremont Island, and PV—Pineview. Location of section line for Fig. 3 indicated. Modified from Hintze (1981) and Coogan and King (1998).

inclusion data recording elevated fluid pressures and peak temperatures of about 300–400 °C at depths of 10–15 km near the base of the sheet (Yonkee et al., 1989). Temperatures cooled as the thrust sheet was emplaced and eroded.

3. Large-scale structural geometry of the Willard thrust sheet

The Willard thrust sheet is well exposed in northern Utah where younger uplift and erosion above the Wasatch anticlinorium and in footwalls of Cenozoic normal faults has exhumed a wide range of structural levels, providing an excellent, composite down-plunge view of this large, far-traveled thrust sheet (Figs. 2B and 3). The sheet contains a 10–15-km-thick package of rocks that includes a lower section of micaceous Neoproterozoic strata, a middle section of quartz-rich upper Neoproterozoic to lower Cambrian strata, and carbonate-rich Paleozoic strata. Neoproterozoic to Mississippian strata thicken overall west-northwestward, whereas Pennsylvanian to Permian strata thicken abruptly southwestward along the margin of the NNW-trending Oquirrh Basin in the central part of the sheet (Royse, 1993). The Willard thrust has a stair-step geometry with a western flat at the base of micaceous Neoproterozoic strata, a composite ramp through quartz-rich upper Neoproterozoic to lower Cambrian strata, a central flat in Cambrian shale and limestone, a central ramp from Cambrian to lower Jurassic strata, and an eastern flat in Jurassic evaporite-bearing strata. The sheet is cut by a central imbricate thrust and several smaller-displacement faults. The Willard sheet displays large-scale fault-bend and fault-propagation folds, locally modified by shear near the main thrust and central imbricate. A major fold train developed east of the leading edge of the Willard thrust above a detachment in Jurassic strata, as a component of thrust slip was transferred eastward into footwall shortening.

Upper levels of the sheet are relatively little deformed, but internal deformation increases downward and westward, with development of cleavage, minor folds, and minor fault and vein arrays (Fig. 4) (Crittenden, 1972; Yonkee, 1997). Cleavage defines an overall asymptotic pattern, ranging from weakly developed and steeply dipping at intermediate distances from the thrust, to moderately to strongly developed and overall gently dipping at lower levels, to intensely developed subparallel to the thrust at the base of the sheet (Fig. 3). In detail, cleavage also refracts to shallower dips and is more strongly developed in mica-rich slate layers. Minor folds range from open and upright at intermediate distances from the thrust, to closed and inclined near the thrust. These patterns reflect varying components of thrust-parallel simple shear and thrust-parallel shortening to extension. Within the western and eastern parts of the sheet, regional folds and cleavage traces trend NNE, approximately perpendicular to the overall ESE transport direction. Within the central part of the sheet, however, early minor folds and cleavage traces trend NNW, oblique to the overall transport direction, and are locally overprinted by NNE-trending folds and crenulation cleavage. These patterns are interpreted to record early internal deformation partly controlled by local stratigraphic variations along the NNW-trending margin of the Oquirrh Basin, followed by deformation during major ESE slip on the Willard thrust.

4. Style and mechanisms of internal deformation

Lithologic characteristics of strata, along with thermal and fluid conditions, partly controlled the style and mechanisms of internal deformation in the Willard sheet. Paleozoic strata in the upper part of the sheet include: strong dolostone intervals that are little deformed except for widespread fracturing; and relatively weaker limestone and shale intervals with rare spaced cleavage, local minor folds, minor faults, and veins. Spaced cleavage seams and veins in limestone record localized mass transfer deformation.

Upper Neoproterozoic to Cambrian strata in the middle part of the sheet include abundant quartzite, quartz-pebble conglomerate, and minor argillite. This section is relatively strong and little deformed, with rare cleavage in argillite, rare open minor folds, local minor faults, and some veins. Quartz grains in most areas are little deformed with limited undulatory extinction, microcracks, and suturing, reflecting minor plastic deformation, cataclasis, and mass transfer (Fig. 5A). Quartz grains near some vein systems, however, are more deformed with widespread suturing and deformation bands, and quartz grains near faults display more numerous microcracks, similar to patterns described for quartzites of the Canyon Range thrust sheet in central Utah (Ismat and Mitra, 2001).

Micaceous Neoproterozoic strata include slate, diamictite, and greywacke of the Perry Canyon Formation at lower levels of the sheet, with moderately to strongly developed cleavage, widespread minor folds, and vein arrays (Fig. 4). These are overlain by micaceous to arkosic quartzite of the Maple Canyon Formation at intermediate distances from the thrust, with weakly to moderately developed cleavage and more open minor folds. Quartz grains and clasts at lower levels are generally deformed into elliptical shapes, with widespread undulatory extinction, deformation bands, subgrains, local recrystallization, dissolution along margins, and short quartz-mica fibers, recording extensive plastic and mass transfer deformation (Fig. 5B). Slate contains chloritoid porphyroblasts that record a component of overall top-to-E shear, and abundant mica-rich matrix with extensive neocrystallization and mass transfer (Fig. 5C).

The Willard thrust can be viewed as a semi-brittle shear zone including the base of the sheet and a central fault core.

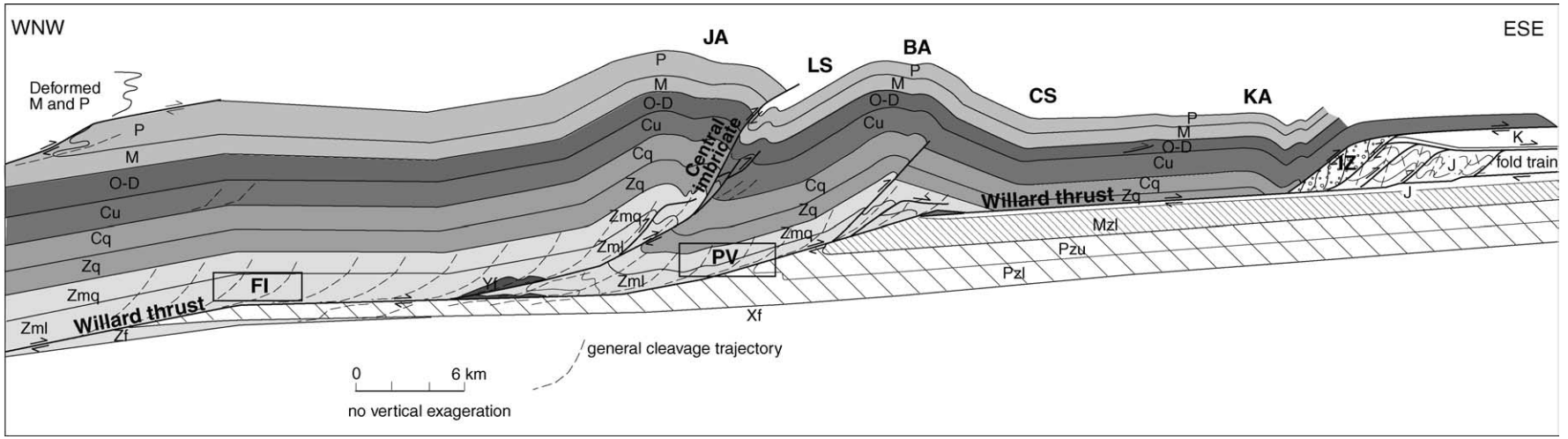

Fig. 3. Generalized cross-section of the Willard thrust sheet incorporating composite down-plunge projections, with effects of Cenozoic normal faulting and tilting above the Wasatch anticlinorium removed. Units in Willard sheet are: Zml—lower level Neoproterozoic micaceous strata (Perry Canyon Formation), Zmq—intermediate level Neoproterozoic micaceous to arkosic quartzite and argillite (Maple Canyon and Kelley Canyon Formations), Zq—upper Neoproterozoic quartz-rich strata, Cq—lower Cambrian quartz-rich strata, Cu—Cambrian carbonate-rich strata, O–D—Ordovician to Devonian strata, M—Mississippian strata, and P—Pennsylvanian to Permian strata. Yf—local, thin slices of Mesoproterozoic(?) Facer Formation at base of Willard sheet. Units in footwall are: Xf—Paleoproterozoic basement rocks, Pzl—lower Paleozoic strata, Pzu—upper Paleozoic strata, Mzl—Triassic to lower Jurassic strata, J—middle Jurassic strata, and K—Cretaceous synorogenic deposits. The Willard thrust sheet displays a ramp-flat geometry, imbricate thrusts, and large-scale folds. Cleavage trajectories, indicated by dashed lines, rotate into parallelism with the thrust at the base of the sheet. See Fig. 2 for study area locations and fold names.

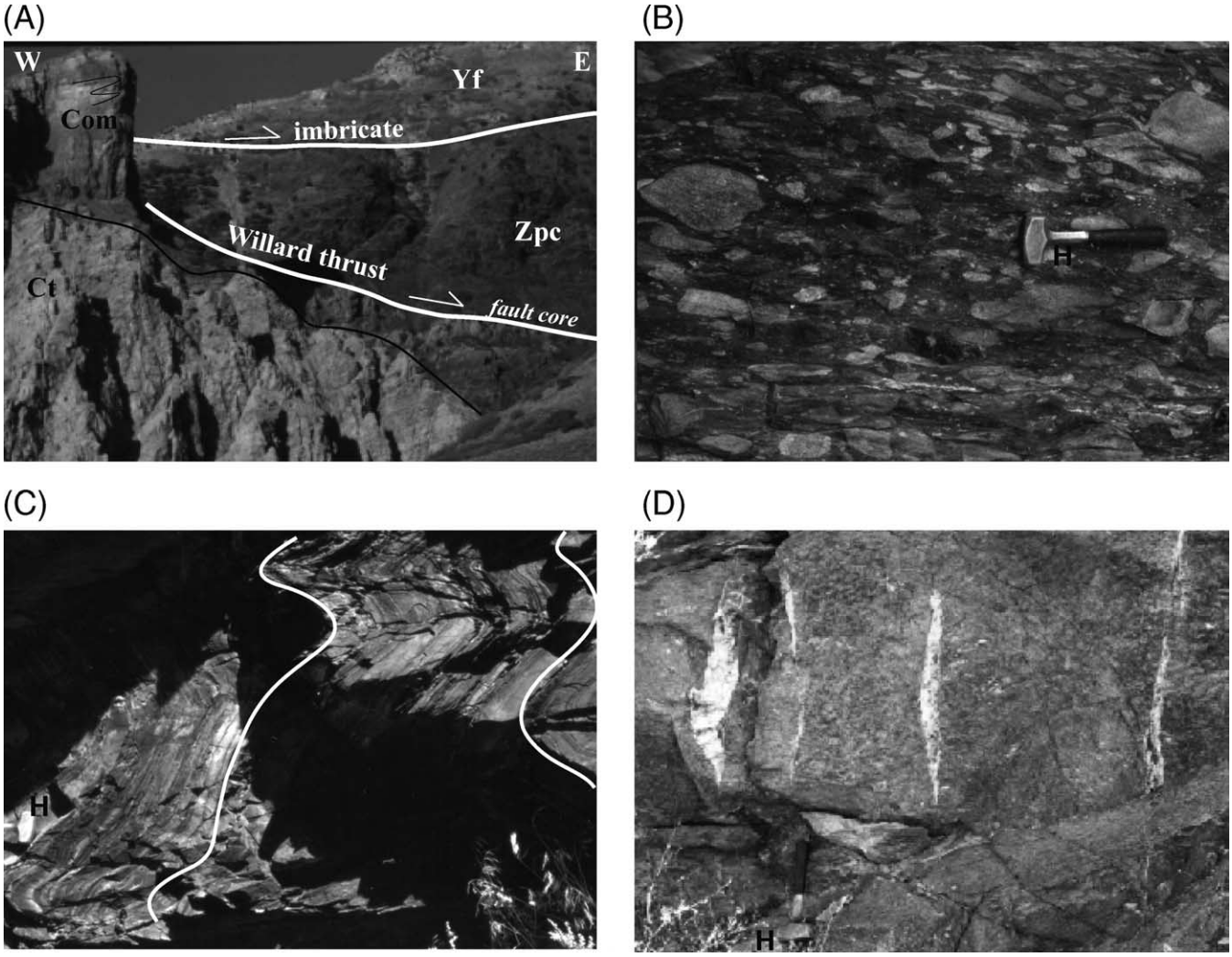

Fig. 4. Mesoscopic structures. (A) View to north of Willard thrust exposed in footwall of the Wasatch normal fault. Fault core of mylonite and cataclasite is locally exposed in steep slopes, and is overlain by strongly deformed slate, greywacke, and diamictite of Neoproterozoic Perry Canyon Formation (Zpc). A slice of Mesoproterozoic(?) Facer Formation (Yf) is repeated above an imbricate thrust. Footwall contains tectonized Cambrian Ophir Shale and Maxfield Limestone (Com), underlain by less deformed Cambrian Tintic Quartzite (Ct). (B) View to north of gently dipping cleavage and stretched clasts in diamictite of the Perry Canyon Formation. Hammer (H) for scale. (C) View to north of minor folds in interbedded greywacke and slate of the Perry Canyon Formation. Hammer (H) for scale. (D) View to west of steep, east-striking quartz veins in the Perry Canyon Formation. Veins are at high angle to local fold axis. Hammer (H) for scale.

The base of the sheet has intense thrust-parallel foliation that is locally refolded, multiple sets of variably deformed veins, boudinaged quartz layers, and cataclasite zones. The fault core consists of mixed mylonite, phyllonite, and ultracataclasite with highly comminuted to recrystallized matrix, complex microvein networks, variably flattened microbreccia fragments, and discrete slip surfaces (Fig. 5D). Textures record overlapping, repeated episodes of crystal–plastic deformation, fracturing, fluid influx, and sealing. Complex patterns of thrust-parallel foliation, veins, and fault rock textures are consistent with slip concentrated along a very weak zone at elevated fluid pressures with steeply inclined principal compressive stress (Yonkee, 1997).

5. Strain methods

Oriented samples of quartzite, greywacke, diamictite, and slate were collected for strain analysis. Three oriented thin sections were cut approximately perpendicular and parallel to cleavage (and to stretching lineation if present) for each sample, digital photographs of thin sections were taken, and grain outlines were digitized and best-fit grain ellipses calculated using the program Scion Image™ (Fig. 6). Grain shapes were analyzed using the R_f–ϕ and normalized Fry methods to estimate two-dimensional strain for each thin section, and results for three thin sections per sample were combined to calculate best-fit three-dimensional strain ellipsoids. Three-dimensional values, scaled

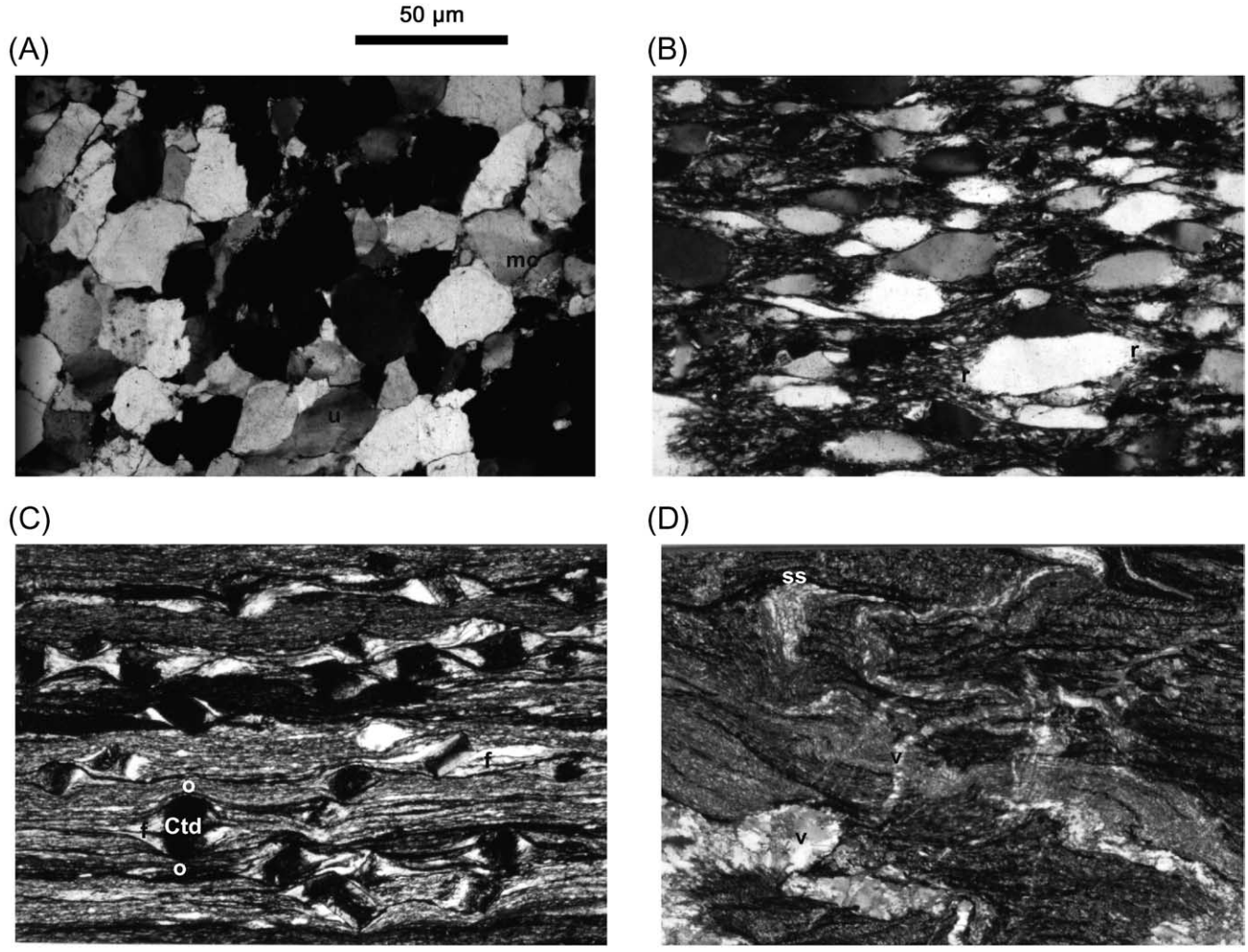

Fig. 5. Microstructures. (A) Upper Neoproterozoic quartzite contains little deformed quartz grains with minor undulatory extinction (u) and limited microcracks (mc). (B) Greywacke from lower level of Willard sheet contains plastically deformed quartz grains with some recrystallized (r) margins and tails, and a micaceous matrix. (C) Slate from lower level of Willard sheet contains chloritoid porphyroblasts (Ctd) with a component of top-to-right (east) shear, sitting in fine-grained micaceous matrix with strong cleavage. Strain caps enriched in opaques (o) and strain shadows with quartz fibers (f) record mass transfer. (D) Phyllonite from Willard thrust fault core. Very fine-grained, recrystallized micaceous matrix displays intense foliation that is refolded and cut by multiple sets of variably deformed veins (v) and slip surfaces (ss).

for volume change, were then factored into pure and simple shear strain components. These steps are briefly described below.

5.1. Lithologies and types of markers

Quartzite is typically micaceous to arkosic and consists of 60–80% sand-size quartz grains, with some larger polycrystalline clasts in conglomeratic layers, 10–20% variably altered feldspar grains, and 10–20% fine-grained micaceous matrix. Quartz grains in less deformed samples have approximately random initial orientations. Strain was estimated using the R_f–ϕ and normalized Fry methods for quartz grains. About 100 grains were measured for most thin sections, which yielded well-constrained, similar results for both methods, indicating that strain values were representative of bulk rock strain.

Greywacke typically consists of 40–70% sand- to granule-size quartz grains and minor lithic clasts, 10–20% altered feldspar grains, and 20–40% fine-grained micaceous matrix (Fig. 6A). Quartz grains in less deformed samples vary from having approximately random initial orientations to having preferred orientations of longer grains along bedding. Samples with distinct bedding fabrics and associated asymmetry of deformed grain orientations relative to cleavage were not used for strain analysis. Strain was estimated using the R_f–ϕ and normalized Fry methods for quartz grains. About 100 grains were measured for most thin sections, which yielded well-constrained results for the R_f–ϕ method, and similar, but less well-constrained, results for the Fry method. Micaceous matrix may have higher strain compared with quartz grains, whereas feldspar grains appear to be less deformed.

Diamictite typically consists of 20–40% granule- to

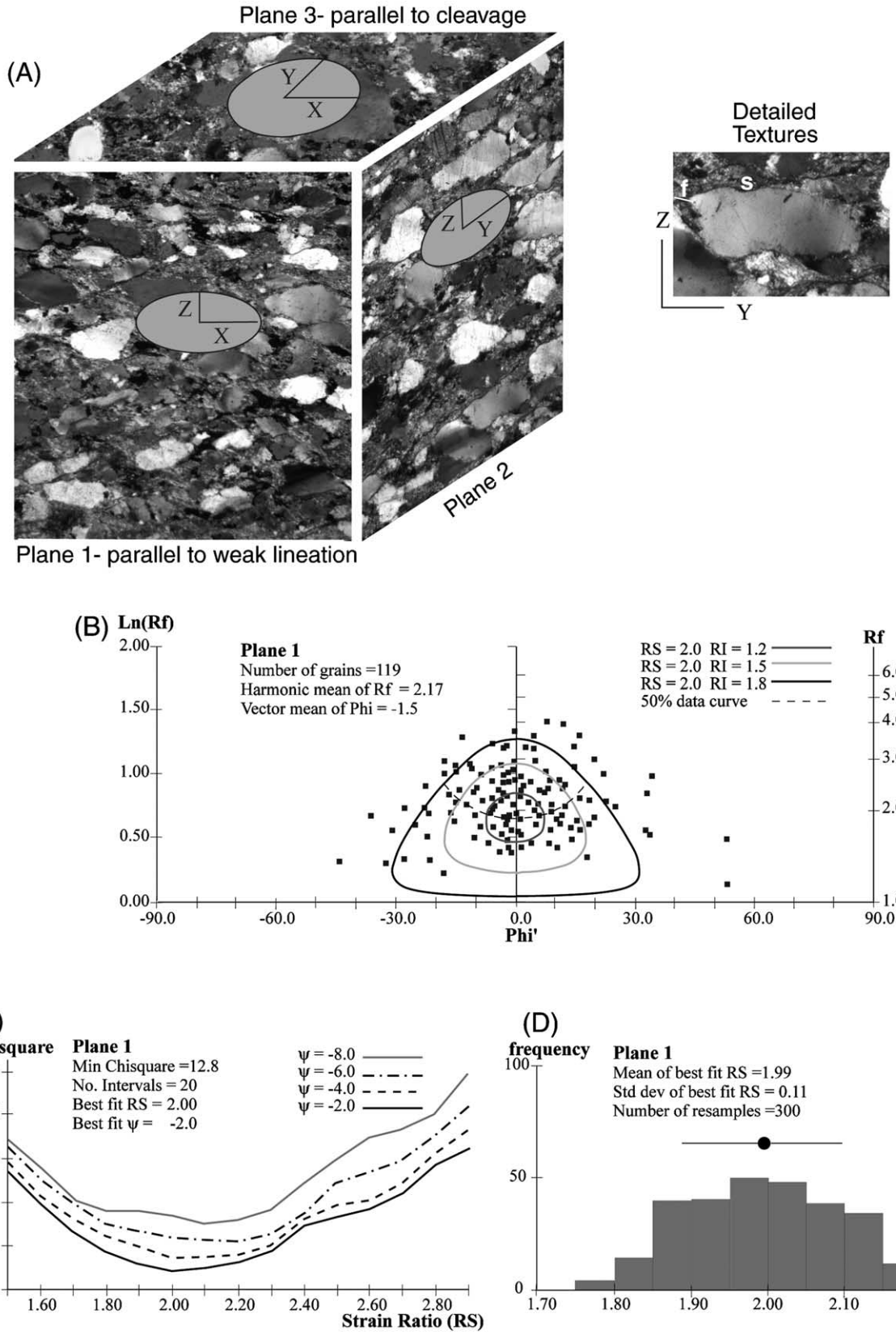

Fig. 6. Strain analysis example. (A) Photomicrographs and two-dimensional strain ellipses estimated from quartz grains for greywacke sample from Pineview study area. Thin sections cut approximately parallel to principal strain planes. Inset of microtextures shows short fibers (f) related to minor extension in the *Y* direction and diffuse seams (s) related to dissolution in the *Z* direction. (B) R_f–ϕ plot for plane 1 with angles plotted relative to vector mean of ϕ. Plot is consistent with strain ratio (*RS*) of about 2 and initial ratios (*RI*) of grains mostly from 1.2 to 1.8. (C) χ-square curves for plane 1 give best-fit strain ratio $RS = 2.0$ and long axis angle $\psi = -2°$. (D) Histogram of best-fit strain ratios (*RS*) for bootstrap resamples of plane 1. Estimated uncertainties for *RS* and ψ are ± 0.11 and $\pm 2°$, respectively.

cobble-size micaceous (altered granitic to schistose) clasts, with minor quartzite and volcanic clasts, 10–30% sand-size quartz and altered feldspar grains, and 40–60% fine-grained micaceous matrix. Average whole rock mineralogy is about 40% quartz, 40% mica, and 20% feldspar, based on point counts and geochemical data. Micaceous clasts also contain an average of 40% quartz, 40% mica, and 20% feldspar. Bedding is generally absent and clasts likely had approximately random initial orientations. Strain was estimated using the R_f–ϕ method for granule-size micaceous clasts in thin sections. About 20–30 clasts were measured for most thin sections, which yielded reasonably well-constrained results. Micaceous clasts have similar mineralogy as the whole rock, generally lack distinct strain shadows, and were used to approximate bulk strain, similar to the approach used by Czeck and Hudleston (2003). Strain was also estimated for pebble- to cobble-size altered granitic clasts in selected outcrops, which yielded similar values to those from thin sections. In detail, competency contrasts between matrix and various clast types may result in complex strain (Treagus and Treagus, 2002). Sand-size quartz grains display strain shadows and have lower strain compared with micaceous clasts, whereas matrix may have slightly higher strain. Boulders of relatively unaltered (less micaceous) granite and quartzite appear less deformed, but constitute $<10\%$ of diamictite outcrops.

Slate typically consists of $>60\%$ micaceous matrix, with some coarser layers that contain sand-size quartz grains surrounded by mica, and rare pebbly layers that grade into diamictite. Strain was estimated for quartz grains in sandy to pebbly slate layers using the R_f–ϕ method, but this probably underestimates total rock strain.

Strain heterogeneity appeared minor at thin-section scale, based on similar strain values determined for multiple subregions in selected samples. Strain was accommodated by both plastic and mass transfer processes. Most grains and clasts were approximately elliptical, with dissolution/precipitation distributed along grain margins, such that the R_f–ϕ and Fry methods yielded reasonable estimates (Onasch, 1984). Samples with discrete cleavage seams that truncated grains were not used for strain analysis. Strain was not measured for recrystallized samples from the basal fault core and rare hydrothermally altered areas.

5.2. Two- and three-dimensional strain estimates

Two-dimensional strain ratios, R_s, and long-axis directions, ψ, were estimated with the R_f–ϕ method using the unstraining approach of Peach and Lisle (1979). Values were consistent with results obtained using the algebraic approach of Shimamoto and Ikeda (1976) and with shapes of R_f–ϕ plots (Fig. 6B) (Lisle, 1985). The unstraining approach used a grid search of R_s and ψ to find best-fit values that minimized a χ-square statistic measuring differences between undeformed grain ellipse shapes and a random initial distribution of long axes (Fig. 6C). Uncertainties in best-fit values were evaluated using bootstrap resampling. Best-fit R_s and ψ values for bootstrap resamples generally had approximately normal distributions, with standard deviations of about 0.1 in R_s and 2° in ψ for samples with moderate strain ($R_s \sim 2$) (Fig. 6D); samples with lower R_s had larger uncertainties in ψ. Strain ratios and directions were also estimated with the normalized Fry method (Erslev, 1988) using an unstraining approach modified from McNaught (1994), with uncertainties in best-fit values evaluated using bootstrap resampling. The Fry method yielded similar strain estimates as the R_f–ϕ method for quartzite and greywacke samples, but uncertainties were larger for samples containing significant matrix. Because of better-constrained results, values from the R_f–ϕ method were used to estimate three-dimensional strain.

Principal directions and axial ratios (R_{XY} and R_{YZ}, $X > Y > Z$) of three-dimensional strain ellipsoids were estimated from input of two-dimensional R_s and ψ values for three sections using a method modified from Owens (1984). The method minimized differences between input values and calculated two-dimensional section ellipses using a matrix norm. Differences between input and calculated R_s and ψ values were mostly less than 0.1 and 2°, respectively, for sections with moderate strain ratios, indicating good fits between input data and calculated three-dimensional ellipsoids. Confidence intervals for three-dimensional strain values were evaluated using Monte Carlo simulations of input section data, incorporating estimated standard deviations in R_s and ψ values. Principal directions and axial ratios were calculated for each simulated input data set, and results were statistically analyzed. For moderate strain samples, estimated Z directions had 90% confidence cones generally less than 2° and were about parallel to measured cleavage poles. X directions were well constrained in samples with distinct stretching lineations, but had confidence intervals greater than 10° in samples with highly oblate strain ellipsoids ($R_{XY} < 1.1$). Principal axial ratios had 90% confidence intervals generally less than 0.2.

Volume change, Δv, was semiquantitatively estimated using microtextures to evaluate stretch in the Y direction for thin sections cut close to the X–Y and Y–Z planes (Fig. 6A). Relations of microtextures to stretch were interpreted as follows: distinct fibers in the Y direction at ends of clasts-distinct elongation ($Y > 1.1$); short fibers at ends of some clasts-minor elongation ($Y \sim 1.05$); only very short fibers and/or very thin seams at ends of a few clasts-approximate plane strain ($Y \sim 1.0$); and thin seams at ends of some clasts-minor shortening ($Y \sim 0.95$). Given axial ratios and the absolute stretch in one direction, scaled principal stretches can be calculated (Barr and Coward, 1974). For example, a sample with axial ratios $R_{XY} = 1.2$ and $R_{YZ} = 1.5$, and microtextures indicating approximate plane strain, has scaled principal stretches of $X = 1.2$, $Y = 1.0$, and $Z = 0.67$, and thus $\Delta v = -0.2$. Samples with similar lithology for a given part of the Willard sheet had consistent relations

between microtextures and axial ratios. On a Flinn diagram, samples with microtextures indicating approximate plane strain plotted along a line defined by:

$$\ln(1 + \Delta v) = \ln(R_{XY}) - ln(R_{YZ}). \quad (1)$$

Samples with elongation in Y plotted to the right of the line, and samples with shortening in Y plotted to the left, providing a general estimate of volume change for a given lithology. This volume change was then used to calculate scaled principal stretches.

5.3. Strain factorization

Principal directions and axial ratios of the three-dimensional strain ellipsoid, scaled for volume change, were factored into strain (coaxial stretch and non-coaxial shear) components using a normalized velocity gradient tensor, assuming a steady state path with simultaneous pure and simple shear (Tikoff and Fossen, 1993, 1995). In detail, deformation paths may have been more complex, but without detailed incremental strain markers, the velocity gradient tensor provides the simplest approach. Strain components were not factored for samples from fold limbs that may have had more complex histories.

Bedding in the Willard sheet (excluding folded areas) remained overall parallel to the main thrust during deformation, and cleavage refraction between beds records banded deformation, which likely constrains admissible strain components to be parallel and perpendicular to the thrust and bedding. Consider a reference frame defined by: a profile (x_1–x_3) plane perpendicular to the thrust (and bedding) and parallel to a reference shear direction; a longitudinal (x_2–x_3) plane perpendicular to the thrust and perpendicular to the reference shear direction; and a thrust-parallel (x_1–x_2) plane (Fig. 7A). The x_1–x_2 plane for an individual sample was based on local bedding orientation to remove effects of minor post-thrusting warping (generally $<10°$). The reference shear direction (x_1) was based on the average trend of slip lineations on shear surfaces and shear veins in a study area.

Finite strain was factored into the following components, assuming steady-state paths: (1) thrust-parallel stretch in the profile plane (α_1); (2) thrust-perpendicular stretch (α_3); (3) thrust-parallel shear in the reference shear direction (Γ_{13}); (4) thrust-parallel shear perpendicular to the reference direction (Γ_{23}); (5) longitudinal stretch (α_2); and (6) longitudinal (wrench) shear (Γ_{12}) (Fig. 7A). Components Γ_{13} and Γ_{23} were combined into a total thrust-parallel shear (Γ_T) and angle (β) between the reference and maximum shear directions for an individual sample. Generally, Γ_{23} was small such that $\Gamma_T \approx \Gamma_{13}$ and $\beta < 30°$. Components 1–3 involved strain in the profile plane, with components 5 and 6 adding three-dimensional complexities. Most components were reasonably constrained, but thrust-parallel shear and stretch components had large uncertainties where cleavage was at low angles to bedding. Equations used to calculate strain components are given in Appendix A.

For ideal plane-strain, Z and X directions (along with poles to cleavage and stretching lineations) lie in the profile plane, and Y directions are parallel to the fold axis and longitudinal plane (Fig. 7B). However, for general strain incorporating longitudinal shear, Z and X directions (along with cleavage poles and stretching lineations) lie oblique to the profile plane, and maximum shear directions of individual samples may be acute to the reference shear direction. Strain relations for samples lacking significant longitudinal shear were conveniently displayed by plotting: (i) the ratio, R, of the strain ellipse in the profile plane ($R \approx R_{XZ}$); and (ii) the angle, θ, between the thrust and the long axis of the strain ellipse in the profile plane (Sanderson, 1982). This plot was contoured for components of thrust-parallel shear (Γ_T) and stretch ratio (α_1/α_3). Samples with significant longitudinal shear or from fold limbs were not included in these plots.

6. Kinematic analysis of study areas

6.1. Fremont Island area

The Fremont Island area is located in the lower, western part of the Willard sheet, and lies above a hanging wall flat in micaceous Neoproterozoic strata and a footwall flat in middle Cambrian shale and limestone (Fig. 8). The Perry Canyon Formation is well exposed here and includes intervals of: greywacke with minor quartzite; mixed slate, diamictite, and greywacke; mafic lava flows and dikes; and diamictite. The base of the thrust sheet is not exposed on the island, but the Willard thrust is imaged seismically beneath the island (McNeil and Smith, 1992).

Mesoscopic structures in the area include minor folds, cleavage, vein arrays, and shear surfaces that have systematic geometric relations (Fig. 9). Bedding is overall gently dipping (with an average strike and dip of 290°, 15°NE in the eastern part of the area and 250°, 25°NW in the western part of the area, subparallel to the Willard thrust), but is locally rotated into ESE-vergent minor folds. Hinge lines of most minor folds plunge gently NNE, although some folds have more easterly trends that may reflect local dextral shear. The average profile plane for the area, which contains the mean pole to bedding and average slip lineation, strikes ESE and is steeply dipping. Cleavage, defined by flattened clasts and preferred orientation of mica, is overall well developed and moderately NW dipping at acute angles to bedding. In detail, cleavage is partly fanned about minor folds, and is at overall lower angles to bedding and more strongly developed in diamictite compared with greywacke. Cleavage is also locally rotated clockwise to steeper north dips, likely reflecting minor dextral shear. Veins, which are best developed within greywacke and quartzite layers, define three gradational sets: set 1—gently

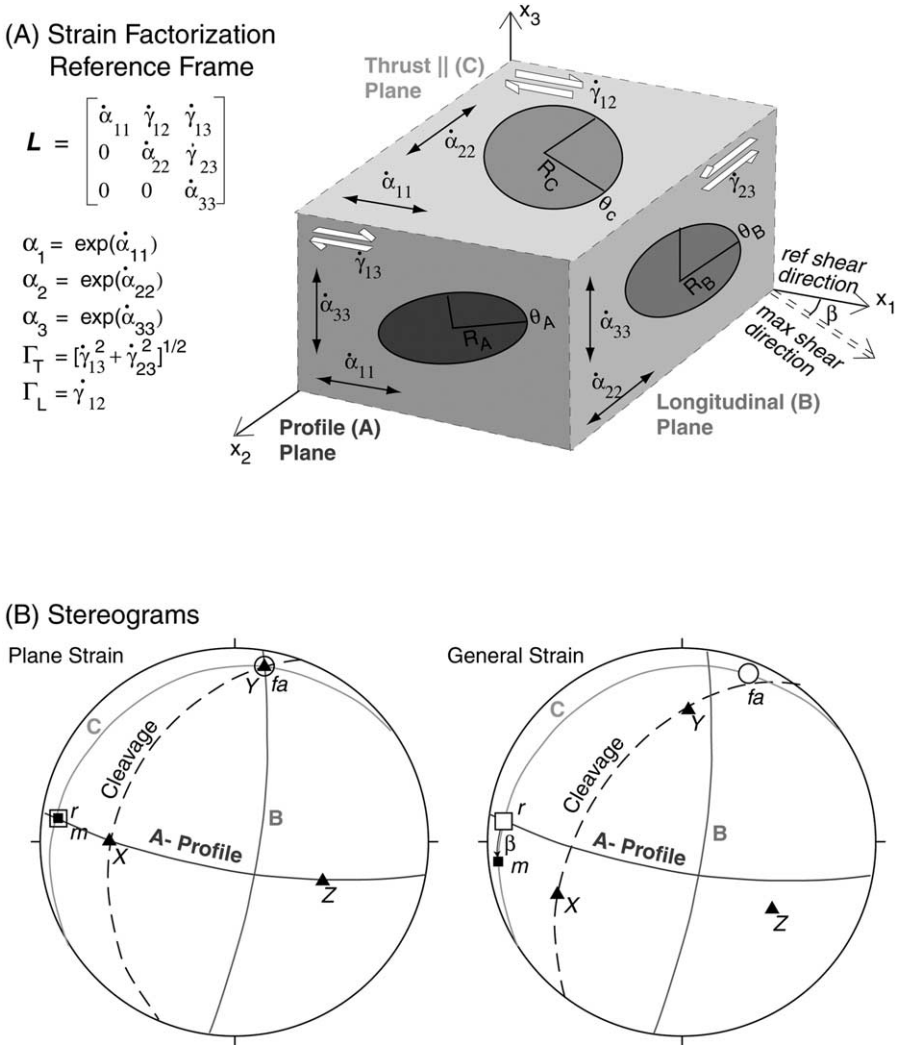

Fig. 7. Strain factorization model. (A) Reference frame and section planes defined by orientations of thrust (and bedding) and reference shear direction. The velocity gradient matrix (**L**), strain components (α_1—thrust-parallel stretch, α_2—longitudinal stretch, α_3—thrust-perpendicular stretch, Γ_T—thrust-parallel shear, and Γ_L—longitudinal shear), and ratios (R) and angles (θ) of two-dimensional section ellipses can be calculated from the three-dimensional strain ellipsoid (see Appendix A). (B) Stereograms illustrating relations between principal strain directions ($X>Y>Z$), cleavage, fold axis (fa), reference and maximum shear directions (r and m), and section planes. For plane strain, X and Z directions lie in the profile plane that is perpendicular to the fold axis. For general strain including longitudinal shear, X and Z directions are oblique to the profile plane. The maximum shear direction for an individual sample may also be at an acute angle, β, to the reference shear direction.

dipping, bed-subparallel veins with top-to-ESE shear; set 2—steeply ESE-dipping veins related to extension about down the dip of cleavage; and set 3—steeply SW-dipping veins related to fold-axis parallel extension and minor dextral shear. Slip lineations on shear surfaces and shear veins trend mostly ESE/WNW at high angles to the fold axis. Weak stretching lineations in diamictite trend WSW to WNW at overall acute angles to cleavage dip. Patterns of mesoscopic structures are consistent with significant top-to-ESE thrust-parallel shear, variable thrust-parallel shortening to extension, minor dextral shear, and minor longitudinal extension (Fig. 9).

Finite strain was estimated for quartz grains in greywacke, micaceous clasts in diamictite, and quartz grains in pebbly slate, with results summarized in Table 1. Principal shortening (Z) directions are moderately to steeply SE plunging, subparallel to cleavage poles (Fig. 10A). Principal stretching (X) directions trend mostly WSW to WNW at overall acute angles to cleavage dips. Y–Z axial ratios range mostly from 1.5 to 2 in greywacke, and from 2 to 3 in diamictite and slate (with overall higher values in slate) (Fig. 10B). X–Y axial ratios are less than 1.5. Microtextures indicate only minor extension to rare minor shortening in the Y direction, consistent with volume losses of about 20% in greywacke and 30% in diamictite (Fig. 10B). Strain ellipses in the profile plane have ratios ($R \approx R_{XZ}$) mostly from 1.5 to 2 in greywacke and from 2 to 3 in diamictite and slate (Figs. 8B and 11). Angles (θ) between bedding and long axes of strain ellipses are mostly from 15 to 35° in greywacke, and from 10 to 25° in diamictite and slate.

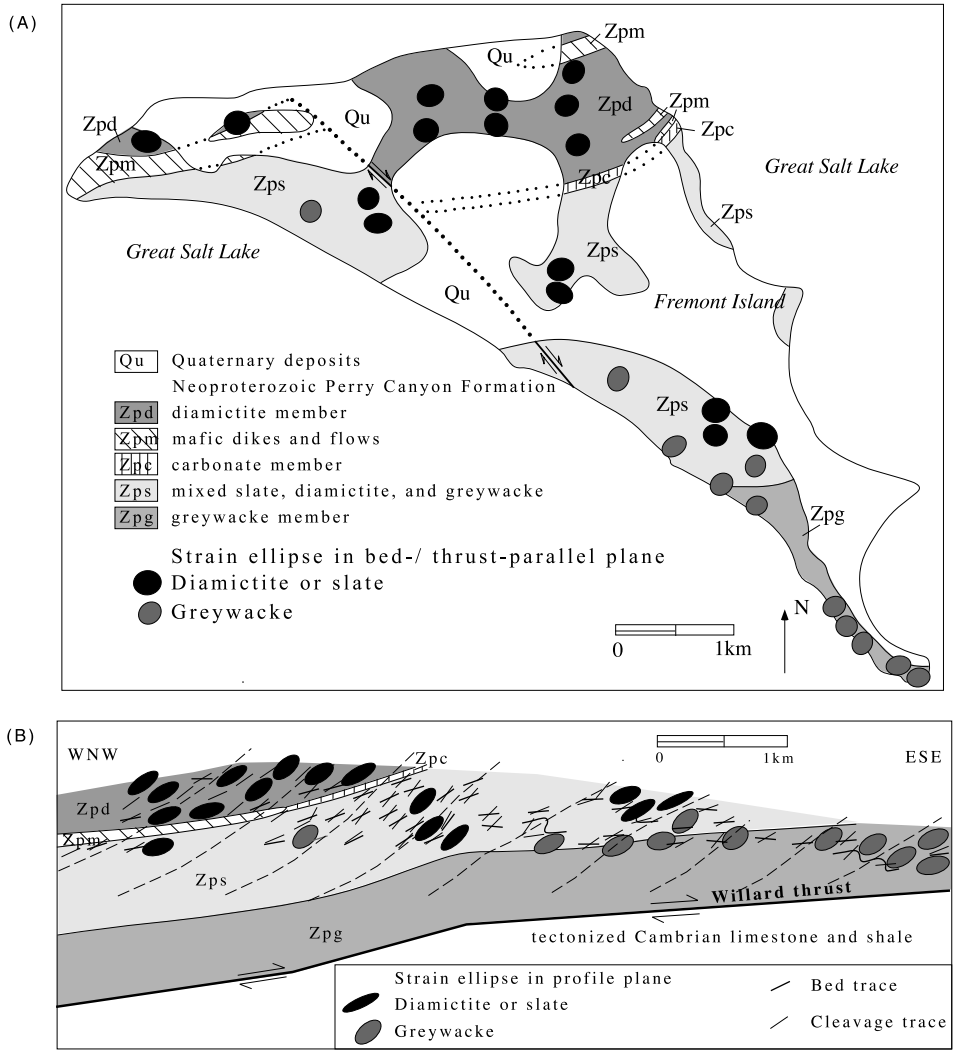

Fig. 8. (A) General geologic map of Fremont Island area illustrating outcrops of different lithologic units. Strain ellipses in bed-parallel planes (or average thrust-parallel plane in folded areas) indicated. (B) Down-plunge projection of Fremont Island area illustrating general structure and cleavage trajectories (dashed lines). Strain ellipses in sample profile planes (which are approximately parallel to the projection plane) indicated. Cleavage and long axes of strain ellipses are at acute angles to bedding and the Willard thrust, with higher ratios in mica-richer diamictite and slate compared with greywacke. Position of Willard thrust based on interpretation of seismic line reported by McNeil and Smith (1992). Projection axis has orientation of 15°, 025°.

Relations between ratios and angles indicate combined thrust-parallel shear and thrust-perpendicular thinning ($\alpha_1/\alpha_3 > 1$). Strain ellipses in bed (and thrust) parallel planes have ratios mostly less than 1.5 and overall NE- to E-trending long axes, reflecting minor longitudinal extension and dextral shear (Fig. 8A).

Three-dimensional finite strain values (incorporating volume change) were factored into strain components (Fig. 12; Table 1). Thrust-parallel stretch in the profile plane (α_1) varied mostly from 0.9 to 1.2, with overall higher values in diamictite compared with greywacke. Thrust-perpendicular stretch (α_3) averaged about 0.7 in greywacke and 0.6 in diamictite, recording significant thinning, especially in mica-rich strata. Thrust-parallel shear (Γ_T) averaged about 0.4 in greywacke to 0.7 in diamictite, with maximum shear directions of individual samples at low angles to the reference shear direction. Longitudinal stretch (α_2) ranged from 1.0 to 1.2 for most samples, reflecting minor extension subparallel to the local fold axis. Some samples had minor dextral longitudinal shear (Γ_L), consistent with clockwise rotation of cleavage to steeper north dips. Longitudinal shear was not concentrated in weak layers, consistent with the combined thrust-parallel and wrench shear model of Ridley (1986). Estimated kinematic vorticity (W) ranged from 0.4 to 0.8 for most greywacke and diamictite samples, with an average of about 0.7 (Table 1). These strain components do not incorporate effects of other structures, including minor folds that produced up to 10% thrust-parallel shortening in some greywacke exposures, and bed-parallel shear veins and surfaces that produced additional thrust-parallel shear.

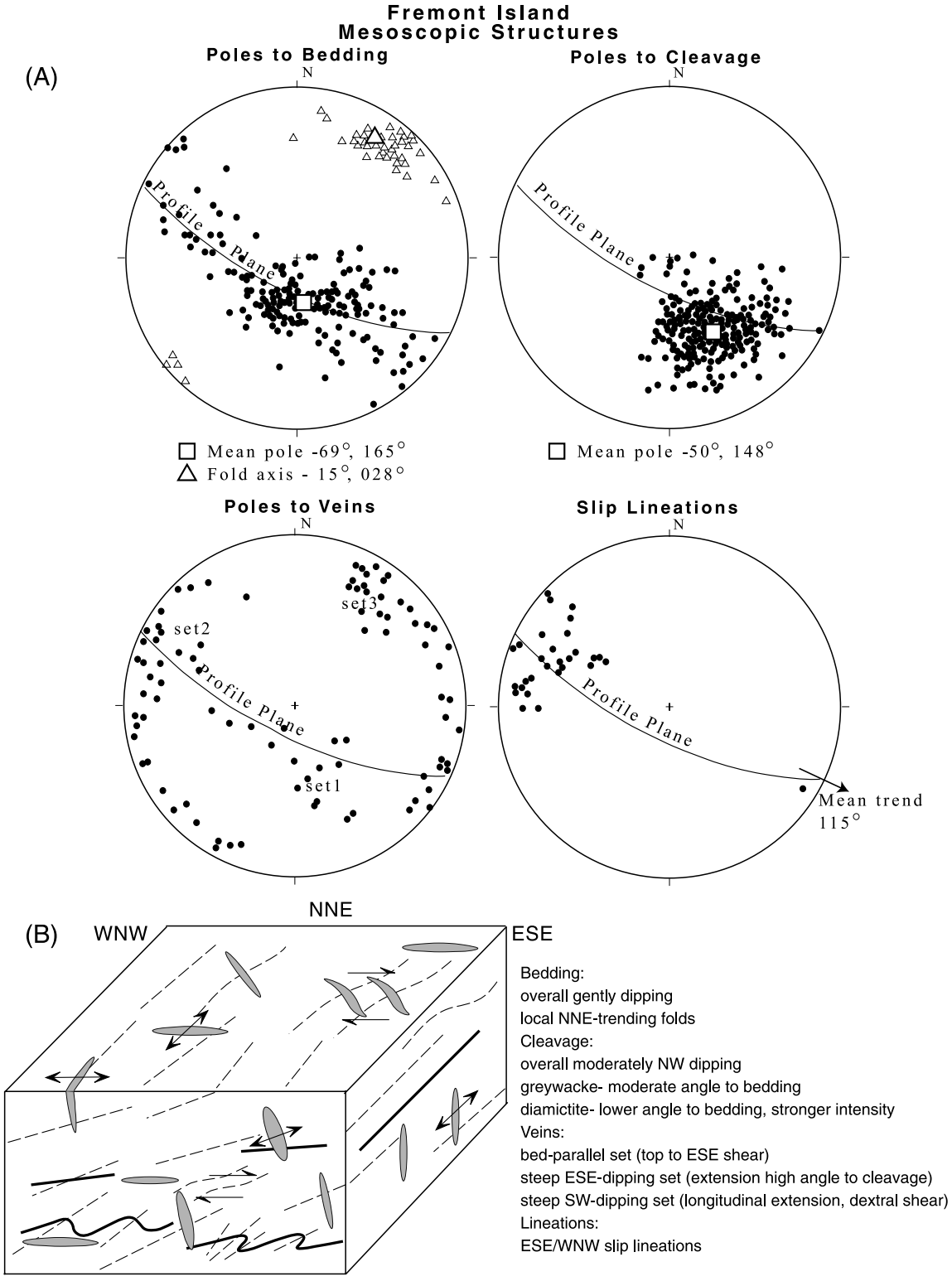

Fig. 9. Geometry of mesoscopic structures in Fremont Island area. (A) Equal-area stereograms. Poles to bedding define a girdle with a gently NNE plunging fold axis, subparallel to hinge lines of most minor folds (small triangles). Poles to cleavage are moderately to steeply SE plunging, corresponding to moderately to gently NW dipping cleavage. Poles to veins define three diffuse sets: set 1 corresponds to veins subparallel to bedding; set 2 to veins at high angles to cleavage; and set 3 to veins at high angles to the fold axis. Slip lineations trend ESE/WNW at high angles to the fold axis. Average profile plane defined by mean bedding pole and slip lineation trend (top toward 115°). (B) Block diagram illustrating general relations of mesoscopic structures. Bedding indicated by solid lines, cleavage by dashed lines, veins by gray, and extension and shear senses by arrows.

Table 1
Strain values for Fremont Island area

Sample[a]	Principal strain values[b]						Scaled strain values[c]				Section ellipses[d]			Factored strain values[e]						
	Z direct	*Y* direct	*X* direct	R_{YZ}	R_{XY}	S_Y	Δv	*Z*	*Y*	*X*	x_1–x_2	*R*	θ	α_1	α_2	α_3	Γ_T	β	Γ_L	*W*
Greywacke																				
FI-1	58, 174	30, 332	10, 068	1.60	1.30	~1	−0.2	0.62	0.99	1.29	290, 20	1.75	23	1.06	1.16	0.67	0.32	14	0.22	0.55
FI-3B	70, 174	17, 326	09, 059	1.39	1.38	s	−0.2	0.67	0.93	1.28	300, 25	1.51	15	1.00	1.14	0.73	0.42	−35	0.23	0.71
FI-4	51, 156	38, 345	05, 252	1.30	1.15	s	−0.2	0.74	0.97	1.11	290, 15	1.38	26	0.98	1.02	0.83	0.29	2	0.17	0.82
FI-8A	53, 152	37, 334	01, 243	1.65	1.17	nd	−0.2	0.63	1.04	1.22	290, 10	1.71	28	0.93	1.14	0.77	0.50	13	0.26	0.81
FI-8B	56, 155	(32, 358)	(10, 262)	1.55	1.07	e	−0.2	0.68	1.05	1.12	*290, 15*	*1.64*	*27*	*folded*						
FI-8C	76, 141	(04, 033)	(13, 302)	1.76	1.02	e+	−0.2	0.63	1.11	1.13	*290, 15*	*1.73*	*16*	*Folded*						
FI-8D	65, 129	22, 334	10, 240	1.77	1.10	e+	−0.2	0.61	1.09	1.20	*290, 15*	*1.81*	*28*	*Folded*						
FI-10A	66, 106	05, 005	23, 272	1.49	1.25	~1	−0.2	0.66	0.98	1.23	*290, 15*	*1.69*	*33*	*Folded*						
FI-10B	79, 161	11, 352	02, 261	1.68	1.29	~1	−0.2	0.60	1.01	1.31	*290, 15*	*1.96*	*12*	*Folded*						
FI-15A	47, 148	(23, 032)	(34, 286)	1.61	1.08	e+	−0.2	0.66	1.06	1.14	290, 20	1.73	34	0.92	1.05	0.84	0.55	10	0.06	0.92
FI-17B	65, 195	(25, 011)	(01, 102)	1.88	1.08	e+	−0.2	0.59	1.11	1.21	265, 20	2.02	16	1.06	1.12	0.68	0.25	3	0.02	0.32
FI-27B	44, 126	30, 001	30, 251	2.02	1.12	e+	−0.2	0.56	1.12	1.26	200, 25	2.14	21	0.97	1.11	0.64	0.64	18	0.18	0.77
FI-68B	46, 136	(44, 318)	(01, 227)	1.75	1.03	e+	−0.2	0.63	1.10	1.14	230, 30	1.71	13	1.00	1.06	0.66	0.38	−8	0.04	0.59
FI-3A-q	75, 165	13, 330	03, 061	1.31	1.24	~1	−0.1	0.75	0.98	1.22	*290, 15*	*1.39*	*15*	*Folded*						
FI-15D-q	53, 183	09, 285	35, 021	1.41	1.15	~1	−0.1	0.73	1.03	1.19	310, 25	1.40	20	0.98	1.17	0.79	0.27	25	0.04	0.80
Average				**1.65**	**1.16**		**−0.2**	**0.64**	**1.04**	**1.20**		**1.74**	**22**	**0.99**	**1.10**	**0.73**	**0.42**	**2**	**0.15**	**0.69**
Diamcitite																				
FI-29A	43, 108	24, 354	37, 244	2.14	1.14	e+	−0.3	0.52	1.10	1.25	190, 35	2.30	13	1.08	1.15	0.57	0.52	9	0.16	0.57
FI-29B	41, 123	03, 030	48, 297	2.14	1.23	e+	−0.3	0.50	1.07	1.31	190, 35	2.58	15	1.14	0.99	0.62	0.78	30	0.22	0.79
FI-40	45, 140	10, 040	42, 300	1.83	1.20	e	−0.3	0.56	1.02	1.23	250, 25	2.17	23	1.00	1.02	0.68	0.70	6	−0.02	0.84
FI-41	38, 160	52, 348	04, 253	1.98	1.12	e+	−0.3	0.54	1.07	1.20	260, 25	2.03	22	0.94	1.06	0.70	0.66	26	0.30	0.85
FI-43	54, 144	35, 335	05, 241	1.83	1.20	e	−0.3	0.56	1.02	1.23	250, 25	1.94	24	1.02	1.14	0.61	0.43	−16	0.14	0.55
FI-56	44, 136	11, 035	44, 294	2.10	1.10	e+	−0.3	0.52	1.10	1.21	260, 25	2.28	25	0.91	1.09	0.70	0.81	−10	−0.15	0.88
FI-58A	47, 151	(26, 035)	(36, 283)	2.49	1.09	e+	−0.3	0.47	1.17	1.28	260, 30	2.71	21	0.96	1.15	0.64	0.95	6	0.09	0.84
FI-58B	52, 159	(35,353)	(07, 260)	2.63	1.07	e+	−0.3	0.45	1.19	1.27	260, 30	2.75	11	1.23	1.20	0.48	0.49	−3	0.08	0.42
FI-59	41, 173	42, 032	21, 282	1.79	1.30	~1	−0.3	0.56	1.00	1.31	260, 30	2.14	16	1.07	1.01	0.65	0.57	18	0.24	0.75
FI-72	55, 161	(30, 012)	(15, 273)	2.51	1.06	e+	−0.3	0.47	1.18	1.25	250, 30	2.64	8	1.19	1.19	0.50	0.41	−8	0.03	0.37
FI-73	49, 167	20, 051	33, 308	2.24	1.20	e	−0.3	0.49	1.09	1.31	260, 30	2.64	19	1.21	1.07	0.54	0.56	33	−0.04	0.53
FI-81	68, 128	17, 348	14, 254	2.37	1.13	e+	−0.3	0.48	1.14	1.29	270, 20	2.53	15	1.04	1.12	0.60	0.86	−30	−0.08	0.79
FI-82	68, 152	17, 014	14, 279	2.16	1.25	e	−0.3	0.44	1.13	1.41	270, 20	3.13	10	1.14	1.06	0.58	0.79	−24	0.06	0.64
Average				**2.17**	**1.16**		**−0.3**	**0.50**	**1.10**	**1.27**		**2.45**	**17**	**1.07**	**1.10**	**0.60**	**0.66**	**3**	**0.08**	**0.68**
Slate																				
FI-17A	54, 144	29, 003	19, 262	2.73	1.14	e+	−0.4	0.41	1.13	1.29	265, 20	3.05	21	0.91	1.16	0.58	1.10	−6	0.07	0.85
FI-27A	56, 124	28, 344	18, 243	2.78	1.10	e+	−0.4	0.41	1.15	1.27	200, 25	2.89	9	1.09	1.17	0.47	0.64	28	0.24	0.77
FI-64	46, 112	30, 343	28, 234	2.25	1.18	e	−0.4	0.46	1.05	1.23	190, 30	2.36	16	0.96	1.15	0.55	0.66	20	0.26	0.68
FI-68A	40, 129	(14, 231)	(47, 339)	2.88	1.04	e+	−0.4	0.41	1.19	1.24	*260, 25*	*3.00*	*20*	*Folded*						
Average				**2.66**	**1.12**		**−0.4**	**0.42**	**1.13**	**1.26**		**2.77**	**15**	**0.99**	**1.16**	**0.53**	**0.80**	**14**	**0.19**	**0.77**

[a] Sample numbers listed by lithology. Samples of quartzite interlayered with greywacke are labeled with q, and not included in average values for greywacke.
[b] Principal axial ratios, R_{XY} and R_{YZ}, are for $X>Y>Z$. *X* and *Y* directions for samples with $R_{XY}<1.1$ are poorly constrained and shown in parentheses.
[c] Scaled stretches, *X*, *Y*, and *Z*, and volume change for given lithology, Δv, based on microtextures used to interpret stretch in *Y* direction (S_Y) with e+—distinct elongation, e—minor elongation, ~1—approximate plane strain, s—minor shortening.
[d] Section ellipse ratio, *R*, and angle, θ, in profile plane calculated for local reference frame with x_1 trending 115, and x_1–x_2 plane parallel to listed bedding orientation (or average thrust orientation in folded areas with values shown in italics; folded areas not included in averages).
[e] Factored strain values calculated using local reference frame, excluding folded areas. See Fig. 7 for explanation of symbols. Γ_L positive for dextral shear. *W*—mean kinematic vorticity number.

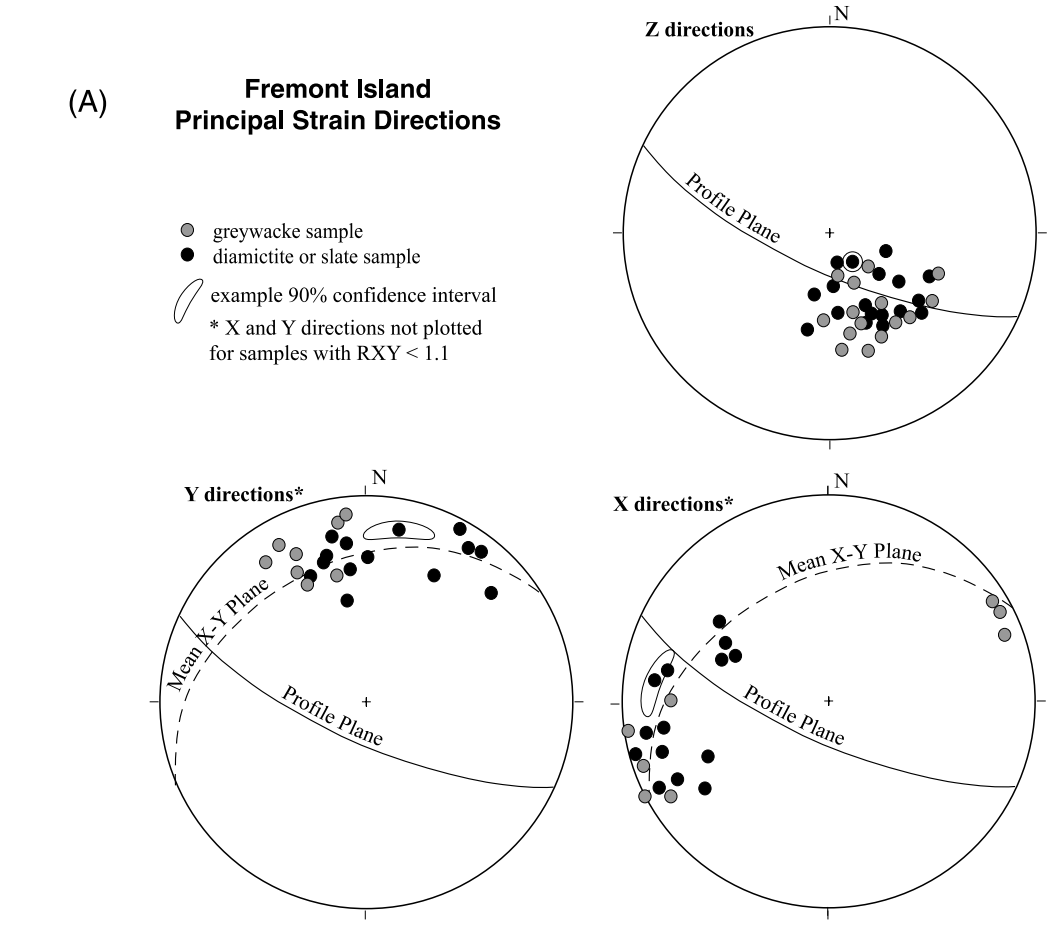

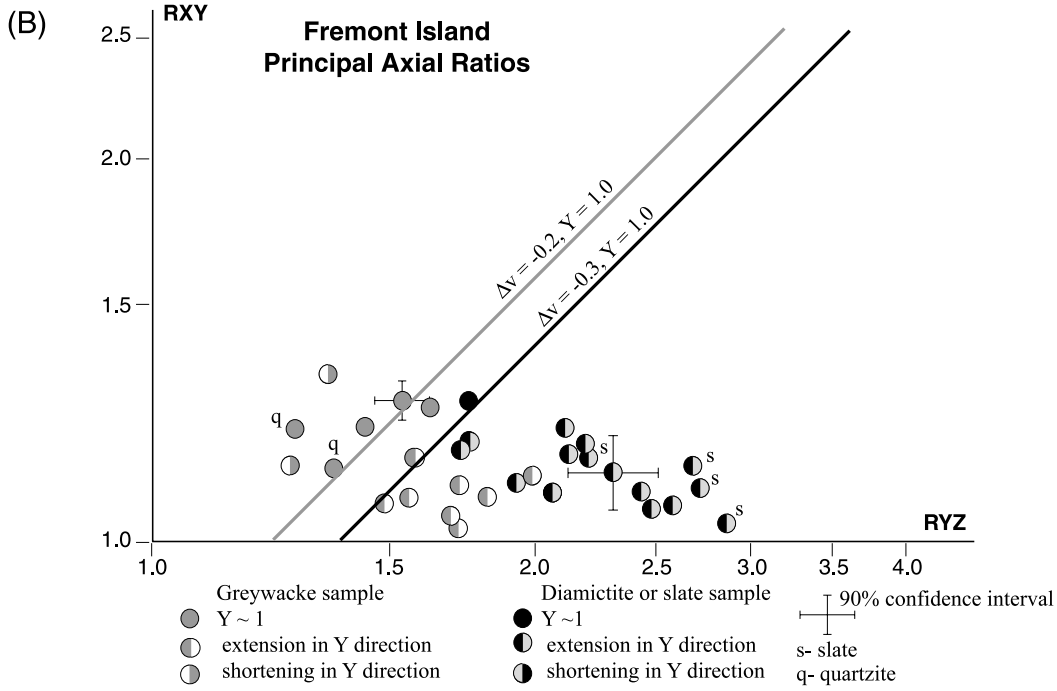

Fig. 10. Principal strain values for Fremont Island area. (A) Equal-area stereograms of principal strain directions ($X>Y>Z$) for diamictite and slate (black circles) and greywacke (gray circles). Z directions are moderately to steeply SE plunging, subparallel to cleavage poles. X directions trend WSW–WNW, overall acute to strike in the X–Y plane. X and Y directions not plotted for samples with $R_{XY}<1.1$. Example 90% confidence intervals indicated. (B) Flinn diagram showing principal X/Y and Y/Z axial ratios (R_{XY} and R_{YZ}). Samples plot in the apparent flattening field, but microtextures in the Y direction indicate varying minor extension to minor shortening. Bold lines indicate strain ratios for various values of volume change, Δv, and plane strain ($Y=1$). Strain ratios and microtextures are consistent with about 20% volume loss in greywacke, and about 30% volume loss in diamictite.

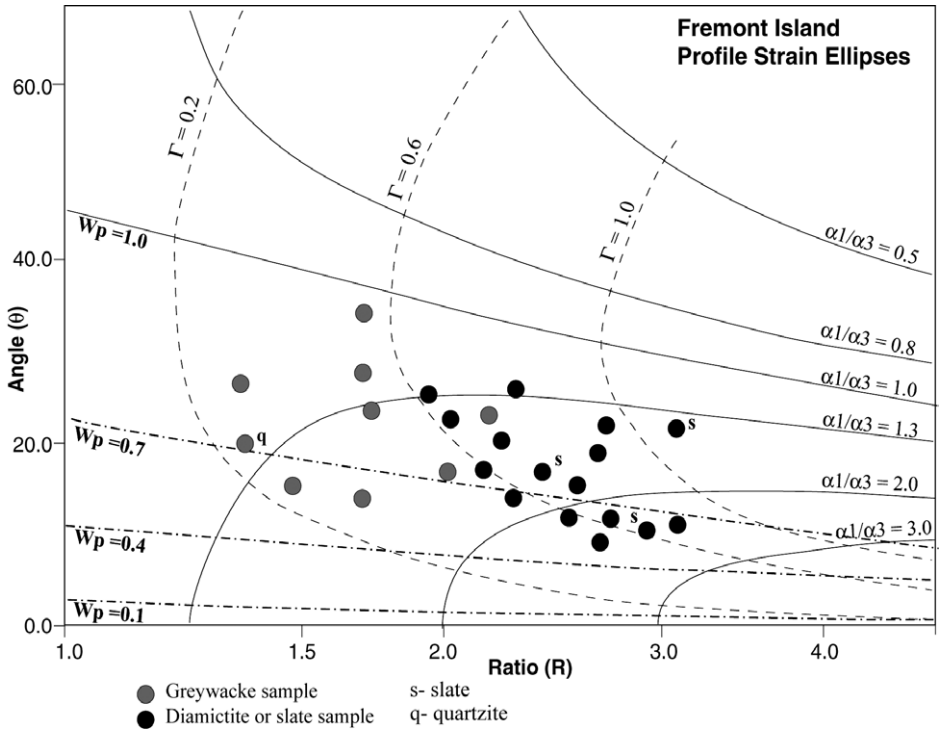

Fig. 11. Plot of strain ratio, R, and angle, θ, between ellipse long axis and bedding in profile plane for samples from Fremont Island area. Contours of thrust-parallel shear (Γ), ratio of thrust-parallel stretch to thrust-perpendicular stretch (α_1/α_3), and kinematic vorticity for plane strain ($W_P = \Gamma/\mathrm{sqrt}[(\ln(\alpha_1/\alpha_3))^2 + \Gamma^2]$) indicated. Samples have moderate to high strain ratios and stretching directions at moderate to low angles to the thrust, with overall higher R and lower θ for diamictite and slate compared with greywacke. Samples from folded areas or with significant longitudinal shear not plotted.

6.2. Pineview area

The Pineview area is located in the lower, central part of the Willard sheet, and lies above a hanging wall flat in micaceous Neoproterozoic strata and a footwall ramp from Cambrian to Mississippian strata (Fig. 13). The Willard thrust currently dips gently ENE, having been rotated on the east limb of the Wasatch anticlinorium; the thrust initially dipped gently west in this area. Footwall cutoffs trend roughly NNE, but in detail the footwall is strongly deformed (Evans and Neves, 1992). Hanging wall rocks in this area include a mixture of greywacke, slate, minor diamictite, and minor quartzite of the Perry Canyon Formation at lower levels, overlain gradationally by micaceous to arkosic quartzite of the Maple Canyon Formation at intermediate distances from the thrust.

Mesoscopic structures in the area include minor folds, cleavage, vein arrays, and shear surfaces that display systematic geometric relations (Fig. 14). Bedding is overall gently dipping (with an average strike and dip of 330°, 30°NE, subparallel to the Willard thrust), but is locally rotated into ENE-vergent minor folds. Bedding poles define a partial girdle with a gently NNW plunging best-fit fold axis. The average profile plane for the area, which contains the mean pole to bedding and mean slip lineation, strikes ENE and is steeply dipping. Cleavage, defined by flattened clasts and preferred orientation of mica, is intense at basal levels adjacent to the thrust, moderately to strongly developed in greywacke and slate at lower levels, and weakly to moderately developed in overlying micaceous quartzite. Cleavage poles plunge steeply to moderately E, corresponding to overall gently dipping cleavage at low angles to bedding in mica-rich strata at lower levels, and moderately W-dipping cleavage at high angles to bedding in quartzite at intermediate levels. In detail, cleavage is refracted to lower angles and more intensely developed in slate layers. Some cleavage poles lie off the profile plane, possibly reflecting minor components of sinistral and dextral shear. Widespread veins within greywacke and quartzite define three partially gradational sets: set 1—gently dipping, bed-subparallel veins related to top-to-ENE shear; set 2—overall steeply SW-dipping veins related to extension at high angles to cleavage in greywacke; and set 3—overall steeply SE-dipping veins related to extension at high angles to the fold axis with local components of sinistral and dextral shear in en échelon arrays. Slip lineations on shear surfaces and shear veins trend ENE/WSW at high angles to the fold axis. Cleavage locally displays weak ENE/WSW-trending stretching lineations, overall subparallel to the profile plane. Patterns of mesoscopic structures are consistent with top-to-ENE shear, thrust-parallel extension at lower levels to shortening in overlying quartzite, limited dextral and sinistral shear, and minor longitudinal extension (Fig. 14). Note, NNW-trending

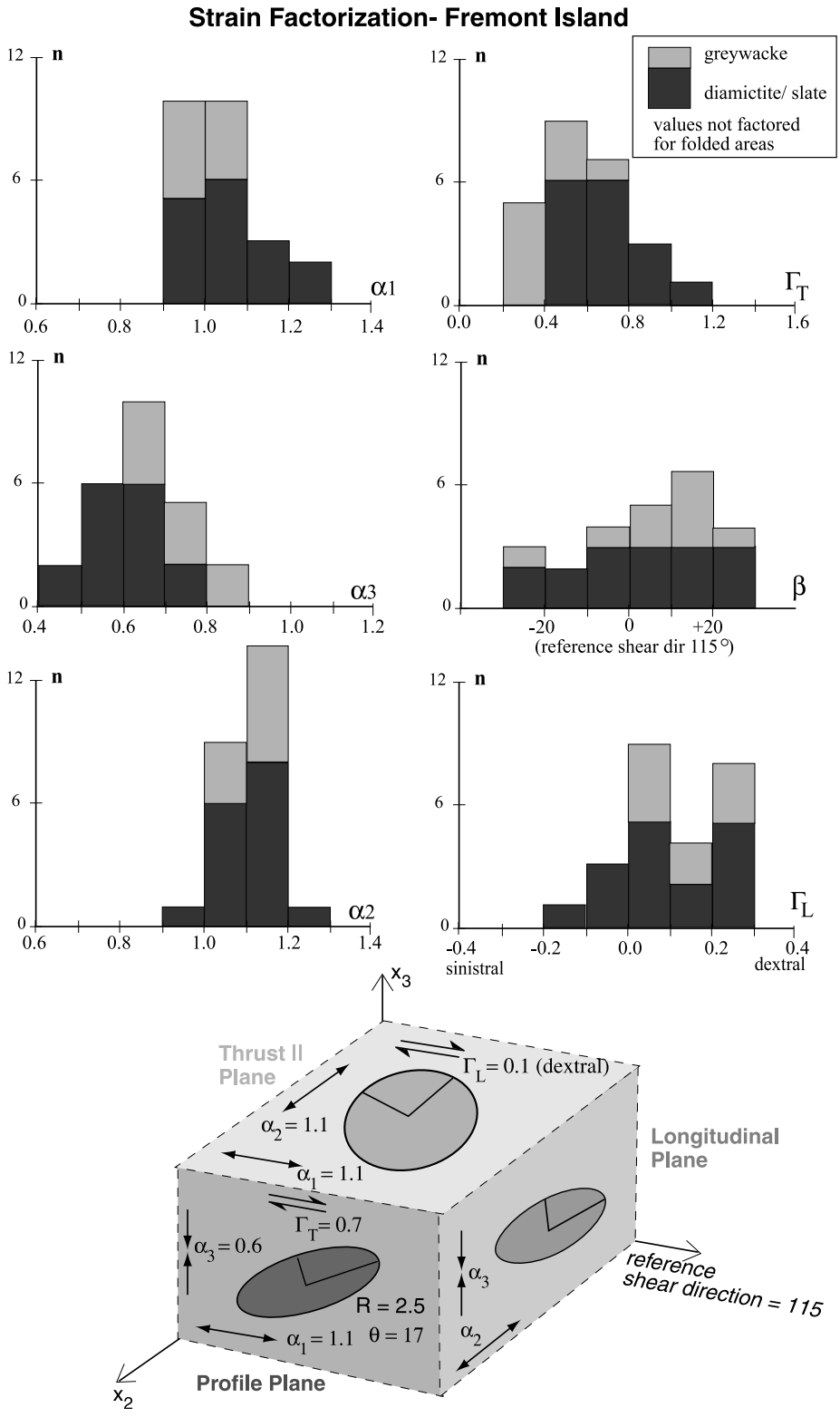

Fig. 12. Strain factorization for Fremont Island area. Histograms show numbers of greywacke (gray), and diamictite and slate (black) samples with various ranges of thrust-parallel stretch (α_1), thrust-perpendicular stretch (α_3), longitudinal stretch (α_2), thrust-parallel shear (Γ_T), angle between reference and sample maximum shear direction (β), and longitudinal shear (Γ_L). Block diagram shows average values of strain components and section ellipses for diamictite. Samples from folded areas not included. See Fig. 7A for definition of factored strain components.

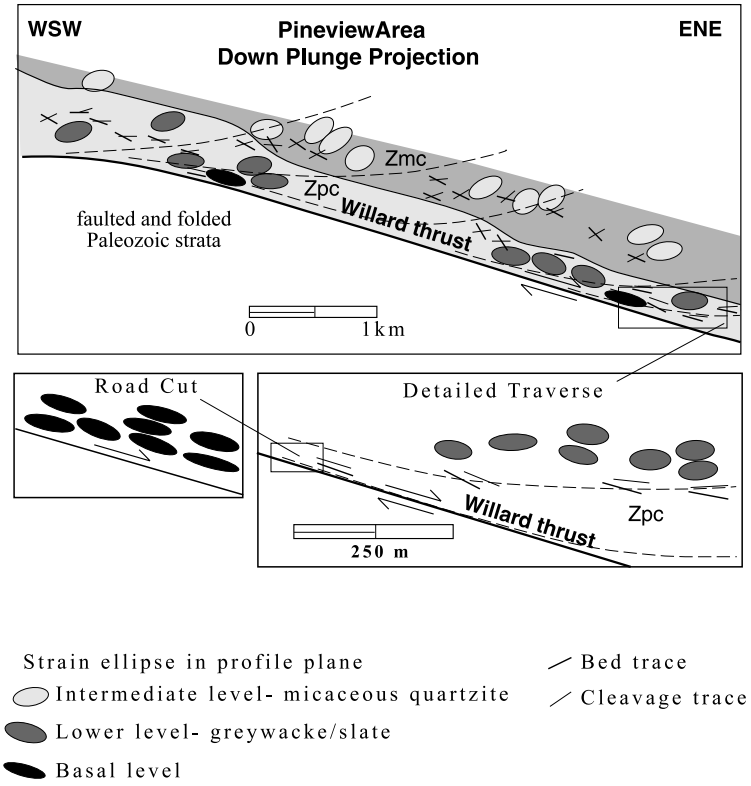

Fig. 13. Down-plunge projection of Pineview area illustrating general structure and cleavage trajectories (dashed lines). Strain ellipses in sample profile planes (which are approximately parallel to the projection plane) indicated. Inset shows results for a detailed traverse near the base of the sheet. Cleavage and long axes of section ellipses rotate into parallelism with the Willard thrust, and strain ratios increase toward the base of the sheet. Projection axis has orientation of 02°, 345°.

cleavage and minor fold axes in this area are oblique to the overall ESE transport direction of the Willard sheet, reflecting partial decoupling of early internal deformation from later large-scale transport. In the Willard Peak area about 10 km to the north, NNW-trending cleavage and early minor folds are locally overprinted by NNE-trending crenulation cleavage that likely formed during large-scale transport.

Finite strain was estimated using quartz grains in greywacke, pebbly slate, and micaceous to arkosic quartzite, with results summarized in Table 2. Principal shortening (Z) directions plunge steeply in greywacke at basal to lower levels, and moderately E in quartzite at intermediate levels, subparallel to corresponding cleavage poles (Fig. 15A). Principal stretching (X) directions trend mostly ENE/WSW, consistent with principal extension overall down the dip of cleavage. Y–Z axial ratios range mostly from 2 to 3 at basal levels, from 1.5 to 2.5 in greywacke at lower levels, and from 1.3 to 2 in overlying quartzite (Fig. 15B). X–Y axial ratios are mostly less than 1.5, but microtexture indicates only minor extension to minor shortening in the Y direction, consistent with average volume losses of about 40% at basal levels, 20–30% in greywacke at lower levels, and 10% in quartzite (Fig. 15B). Strain ellipses at basal levels have ratios (R) in the profile plane from about 3 to 5 and angles (θ) between bedding and the long axis $<10°$, consistent with intense thrust-subparallel cleavage (Figs. 13 and 16). Greywacke and slate at lower levels have R mostly from 1.5 to 3, and θ from 10 to 30°, reflecting overall moderate-intensity cleavage at acute angles to bedding. Relations between ratios and angles indicate combined thrust-parallel shear and thrust-perpendicular thinning at lower to basal levels ($\alpha_1/\alpha_3 > 1$). Overlying quartzite of the Maple Canyon Formation has R mostly from 1.3 to 2 and θ from 50 to 70°, consistent with lower-intensity cleavage at high angles to bedding, reflecting thrust-parallel shortening and shear. Note that these strain ratios are slightly higher than typical ratios ($R \sim 1.2$–1.5) for the Maple Canyon Formation in more western parts of the Willard sheet where the underlying Perry Canyon Formation is thicker.

Three-dimensional finite strain values (incorporating volume change) were factored into strain components (Fig. 17; Table 2). Thrust-parallel stretch in the profile plane (α_1) averaged about 1.3 at basal levels, 1.1 in greywacke at lower levels, and 0.8 in overlying quartzite, reflecting minor extension to shortening. Thrust-perpendicular stretch (α_3) averaged about 0.5 at basal levels and 0.7 at lower levels, reflecting significant thinning. Thrust-parallel shear (Γ_T) averaged about 0.6 at basal levels (but was poorly constrained), 0.5 in greywacke at lower levels, and 0.3 in overlying quartzite. Longitudinal stretch (α_2) varied from 0.9 to 1.1 for most samples, and longitudinal

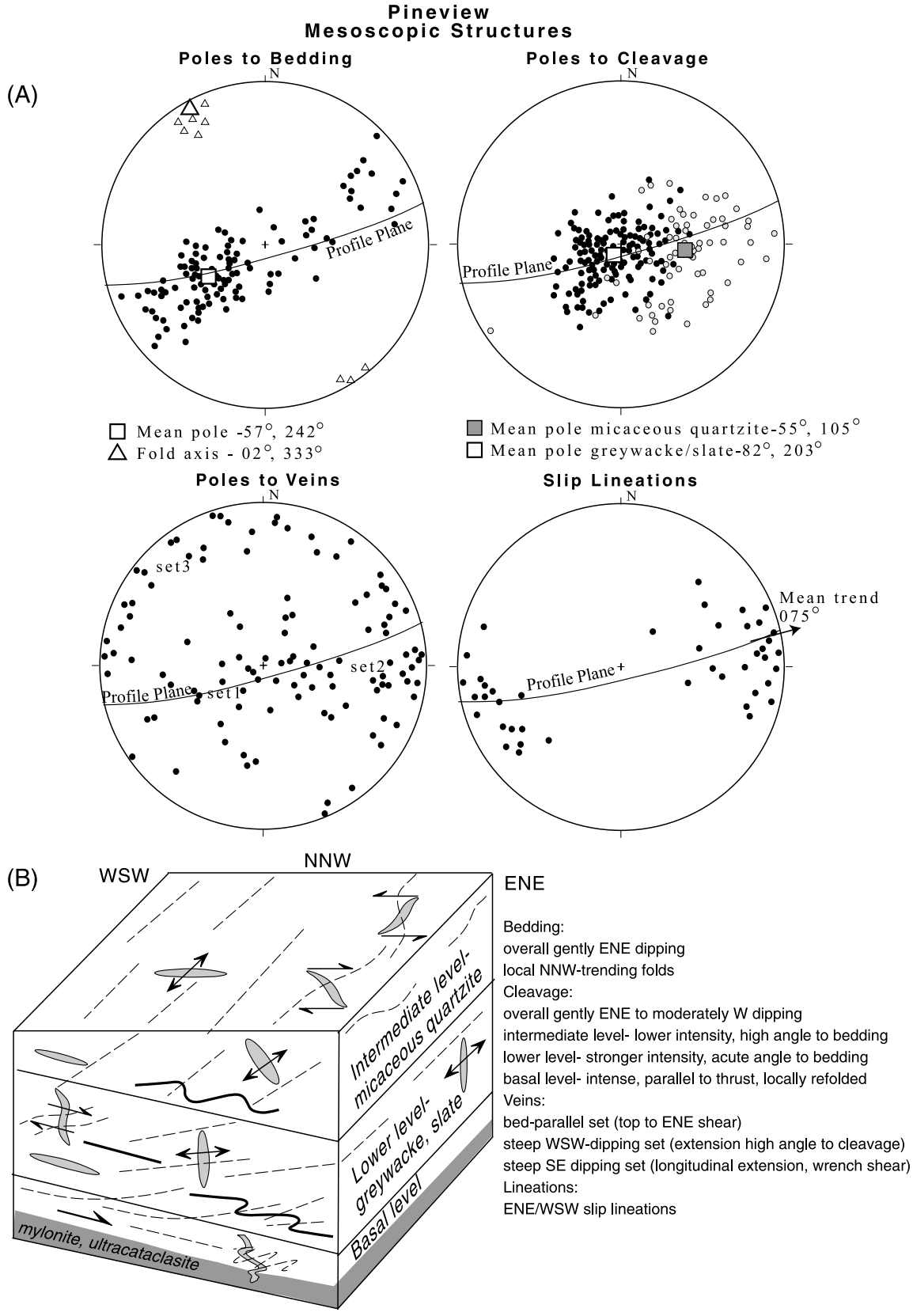

Fig. 14. Geometry of mesoscopic structures for Pineview area. (A) Equal-area stereograms. Poles to bedding define a girdle with a gently NNW plunging fold axis, subparallel to hinge lines of minor folds (small triangles). Poles to cleavage for micaceous to arkosic quartzite at intermediate levels (light gray), and for greywacke and slate at lower to basal levels (black circles) define a partial girdle. Poles to veins define three diffuse sets: set 1 corresponds to veins subparallel to bedding; set 2 to veins at high angles to cleavage; and set 3 to veins at high angles to the fold axis. Slip lineations trend mostly ENE/WSW at high angles to the fold axis. Average profile plane defined by mean bedding pole and slip lineation trend (top toward 075°). (B) Block diagram illustrating general relations of mesoscopic structures at different structural levels in Pineview area. Bedding indicated by solid lines, cleavage by dashed lines, veins by gray, and extension and shear senses by arrows.

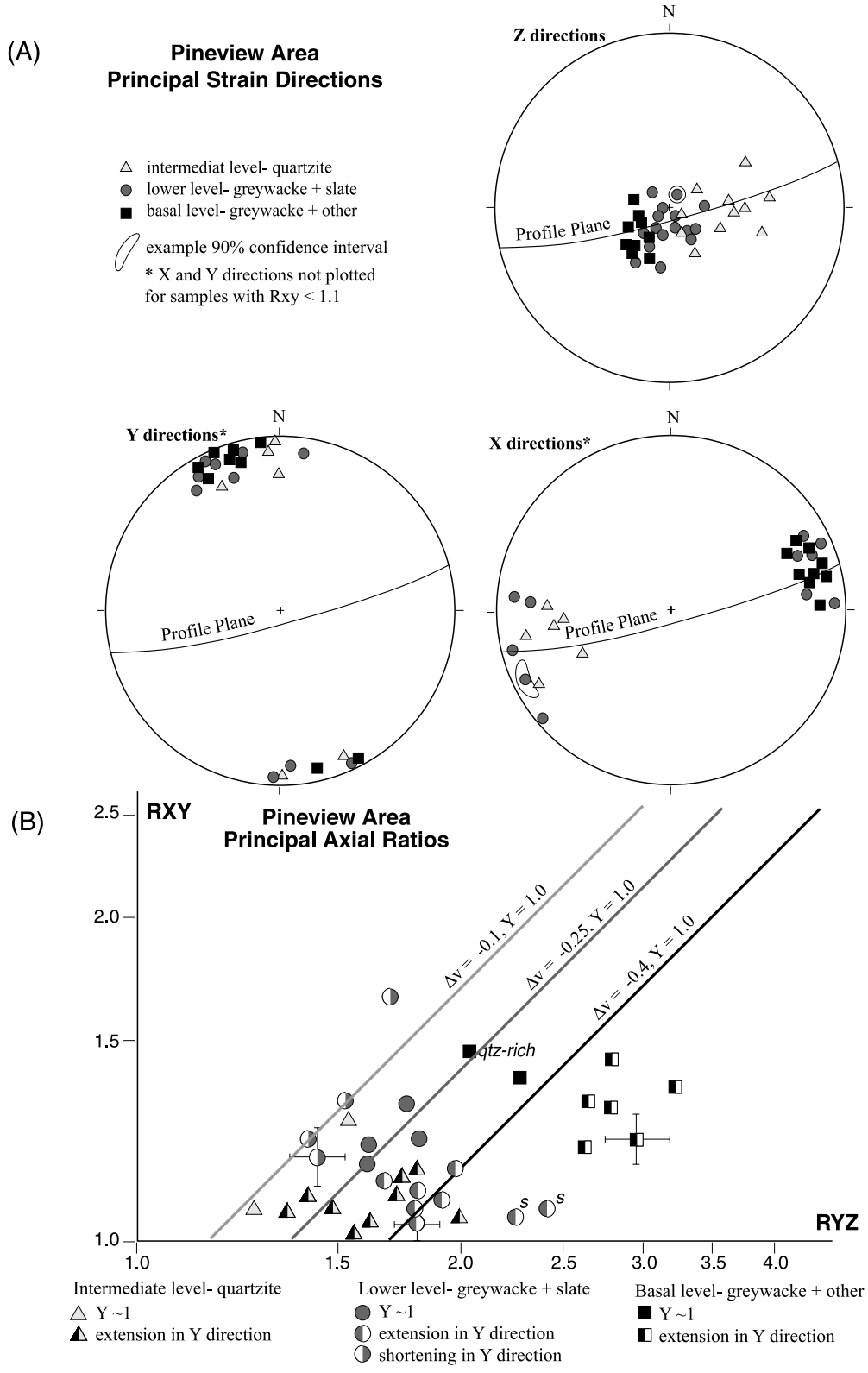

Fig. 15. Principal strain values for Pineview area. (A) Equal-area stereograms of principal strain directions ($X > Y > Z$) for intermediate level micaceous to arkosic quartzite (light gray triangles), lower level greywacke and slate (medium gray circles), and basal level samples (black squares). Z directions are steeply to moderately E plunging, subparallel to cleavage poles. X directions trend ENE/WSW, overall subparallel to the profile plane. Y directions are mostly at low angles to fold axis. X and Y directions not plotted for samples with $R_{XY} < 1.1$. Example 90% confidence intervals indicated. (B) Flinn diagram showing principal X/Y and Y/Z axial ratios (R_{XY} and R_{YZ}). Most samples plot in the apparent flattening field, but microtextures in the Y direction indicate varying minor extension to minor shortening. Bold lines indicate strain ratios for various values of volume change, Δv, and plane strain ($Y = 1$). Strain ratios and microtextures indicate volume losses of about 40% for the basal level, 20–30% for greywacke at lower levels, and 10% for quartzite at intermediate levels. s—slate sample.

Table 2
Strain values for Pineview area

Sample[a]	Principal strain values[b]						Scaled strain values[c]				Section ellipses[d]			Factored strain values[e]						
	Z direct	*Y* direct	*X* direct	R_{YZ}	R_{XY}	S_Y	Δv	*Z*	*Y*	*X*	x_1–x_2	*R*	θ	α_1	α_2	α_3	Γ_T	β	Γ_L	*W*
Basal level																				
W-2A1-g/d	75, 245	01, 335	15, 064	3.22	1.41	e+	−0.4	0.35	1.11	1.57	330, 20	4.57	4	1.01	1.11	0.53	1.51	−11	−0.05	0.86
W-2B1-g	70, 247	02, 151	20, 059	2.78	1.34	e	−0.4	0.39	1.08	1.44	330, 25	3.66	4	1.38	1.09	0.40	0.39	−34	0.15	0.29
W-2B2-g	76, 247	05, 355	13, 088	2.98	1.23	e	−0.4	0.38	1.13	1.39	330, 20	3.62	3	1.30	1.14	0.40	0.56	−15	−0.13	0.39
W-2B4-g	74, 220	09, 342	14, 074	2.64	1.38	e	−0.4	0.40	1.05	1.44	330, 20	3.63	6	1.36	1.03	0.42	0.57	25	0.07	0.41
W-2C3-g	63, 220	05, 330	26, 062	2.20	1.30	e	−0.4	0.46	1.00	1.31	320, 30	2.84	3	1.27	1.03	0.47	0.25	−19	0.11	0.24
W-2D-g	65, 229	12, 345	22, 080	2.63	1.23	e	−0.4	0.41	1.09	1.34	320, 30	3.23	3	1.32	1.11	0.42	0.23	3	−0.04	0.18
W-2E-g	65, 202	15, 330	18, 075	2.27	1.47	~1	−0.4	0.43	0.98	1.43	320, 30	3.22	7	1.26	0.95	0.47	0.60	40	−0.05	0.47
W-21A-g/d	66, 226	10, 340	21, 074	2.80	1.50	e	−0.4	0.37	1.04	1.56	310, 30	4.19	4	1.49	1.01	0.40	0.62	−33	−0.09	0.40
W-2A2-q	73, 288	08, 166	14, 074	2.02	1.55	~1	−0.2	0.50	1.01	1.57	330, 20	3.08	5	1.51	0.99	0.54	0.53	−26	−0.07	0.46
Average				**2.69**	**1.36**		**−0.4**	**0.40**	**1.06**	**1.43**		**3.62**	**4**	**1.30**	**1.05**	**0.45**	**0.59**	**−5**	**−0.01**	**0.41**
Lower level																				
W-3A1-g	75, 220	06, 334	14, 065	1.82	1.27	~1	−0.3	0.55	1.00	1.27	330, 25	2.29	12	1.17	1.02	0.60	0.49	−2	0.10	0.55
W-3B1-g	81, 148	08, 345	03, 255	1.66	1.80	s+	−0.3	0.52	0.87	1.56	330, 15	2.97	17	1.20	0.88	0.69	0.99	5	0.04	0.85
W-3C1-g	70, 209	10, 328	17, 060	1.98	1.25	e	−0.3	0.52	1.04	1.30	330, 25	2.45	8	1.21	1.06	0.56	0.43	10	0.15	0.46
W-3C2-g	77, 318	10, 178	08, 087	1.53	1.37	s	−0.3	0.60	0.92	1.26	330, 20	2.02	13	1.14	0.93	0.67	0.43	−19	−0.23	0.63
W-3D2-g	87, 271	(03, 081)	(01, 171)	1.78	1.05	e	−0.3	0.59	1.06	1.11	330, 15	1.77	12	1.01	1.11	0.63	0.34	−27	−0.03	0.46
W-3E1-g	75, 130	(07, 014)	(13, 282)	1.92	1.09	e	−0.3	0.56	1.07	1.17	330, 10	2.03	19	1.05	1.11	0.70	0.62	29	0.07	0.76
W-3E2-g	82, 024	02, 155	06, 245	1.42	1.27	s	−0.3	0.68	0.95	1.21	320, 10	1.74	15	1.11	0.99	0.73	0.41	−22	0.11	0.68
W-20B-g	77, 141	07, 009	09, 275	1.78	1.13	e	−0.3	0.58	1.03	1.16	330, 10	1.92	15	1.07	1.03	0.66	0.53	15	−0.03	0.67
W-23-g	72, 084	03, 181	18, 273	1.69	1.16	e	−0.2	0.62	1.05	1.22	330, 10	1.93	29	0.91	1.02	0.76	0.64	7	−0.07	0.84
W-25A-g	71, 143	(13, 008)	(13, 275)	1.76	1.07	nd	−0.2	0.59	1.05	1.12	300, 20	1.75	19	0.97	1.13	0.67	0.44	15	0.09	0.60
W-70-g	60, 188	15, 326	25, 064	1.59	1.20	~1	−0.2	0.64	1.02	1.23	340, 35	1.78	24	1.15	0.96	0.66	0.38	34	0.12	0.54
W-71A-g	58, 213	20, 340	23, 080	1.60	1.24	~1	−0.2	0.63	1.01	1.25	320, 35	1.97	7	1.19	0.98	0.64	0.30	23	−0.04	0.41
W-72-g	80, 219	04, 332	09, 063	1.76	1.36	~1	−0.2	0.58	1.01	1.37	320, 20	2.37	11	1.27	0.98	0.59	0.44	−19	0.04	0.48
W-22B-s	85, 260	(04, 110)	(03, 019)	2.44	1.06	e	−0.3	0.48	1.17	1.24	350, 25	2.50	20	0.96	1.25	0.61	0.82	2	−0.09	0.73
W-25B-s	78, 192	(11, 003)	(03, 094)	2.25	1.06	e+	−0.3	0.51	1.14	1.21	300, 20	2.37	9	1.17	1.16	0.54	0.39	3	0.08	0.40
Average				**1.71**	**1.25**		**−0.25**	**0.58**	**1.02**	**1.24**		**2.08**	**15**	**1.11**	**1.01**	**0.66**	**0.50**	**4**	**0.02**	**0.61**
Inter level																				
W-105-q	58, 097	06, 356	32, 263	1.25	1.08	~1	−0.1	0.81	1.01	1.09	325, 30	1.26	62	0.85	1.08	0.98	0.18	7	−0.01	0.58
W-107A-q	88, 132	(01, 350)	(01, 260)	1.58	1.03	e	−0.1	0.70	1.11	1.15	*330, 30*	*1.62*	*31*	*Folded*						
W-109-q	54, 090	02, 357	35, 265	1.61	1.33	~1	−0.1	0.64	1.02	1.36	340, 20	2.03	55	0.76	1.04	1.15	0.15	11	−0.02	0.32
W-110-q	47, 060	03, 153	43, 246	1.75	1.13	e+	−0.1	0.66	1.15	1.29	315, 35	1.88	76	0.69	1.15	1.20	0.26	12	0.23	0.48
W-112-q/g	75, 051	(09, 180)	(11, 272)	1.60	1.04	e	−0.1	0.70	1.11	1.16	345, 35	1.62	68	0.78	1.15	0.99	0.41	−7	−0.10	0.72
W-116-q/g	80, 158	(07, 020)	(06, 289)	1.48	1.07	e	−0.1	0.72	1.07	1.15	330, 40	1.53	42	0.90	1.09	0.91	0.45	9	0.02	0.88
W-283-q	62, 080	05, 180	27, 273	1.80	1.17	e	−0.1	0.62	1.11	1.30	*330, 30*	*1.96*	*55*	*Folded*						
W-286A-q	41, 084	(44, 230)	(17, 338)	1.40	1.10	e	−0.1	0.74	1.04	1.17	315, 35	1.40	76	0.81	1.08	1.03	0.15	22	0.17	0.58
W-286C-q	42, 105	(19, 214)	(41, 323)	1.35	1.06	e	−0.1	0.77	1.04	1.11	315, 35	1.34	75	0.78	1.04	0.99	0.15	17	0.17	0.53
W-289A-q	63, 149	23, 359	15, 260	1.98	1.11	e+	−0.1	0.60	1.19	1.32	*330, 30*	*2.08*	*36*	*Folded*						
W-297-q	65, 108	22, 335	10, 241	1.73	1.17	e	−0.1	0.64	1.10	1.28	*330, 30*	*2.02*	*48*	*Folded*						
Average				**1.58**	**1.12**		**−0.1**	**0.69**	**1.08**	**1.21**		**1.58**	**65**	**0.81**	**1.09**	**1.03**	**0.25**	**10**	**0.06**	**0.58**

[a] Samples grouped by structural level. Lithologies are g—greywacke, d—diamictite, s—slate, q—quartzite, /—transitional. Greywacke is the main lithology at basal and lower levels and used for averages.
[b] Principal axial ratios, R_{XY} and R_{YZ}, are for $X > Y > Z$. *X* and *Y* directions for samples with $R_{XY} < 1.1$ are poorly constrained and shown in parentheses.
[c] Scaled stretches, *X*, *Y*, and *Z*, and volume change for given lithology and level, Δv, based on microtextures used to interpret stretch in *Y* direction (S_Y). See Table 1 for symbols.
[d] Section ellipse ratio, *R*, and angle, θ, in profile plane calculated for local reference frame with x_1 trending 075, and x_1–x_2 plane parallel to listed sample bedding orientation (or average thrust orientation in folded areas with values shown in italics; folded areas not included in averages).
[e] Factored strain values calculated using local reference frame, excluding folded areas. See Fig. 7 for explanation of symbols. Γ_L positive for dextral shear. *W*—mean kinematic vorticity number.

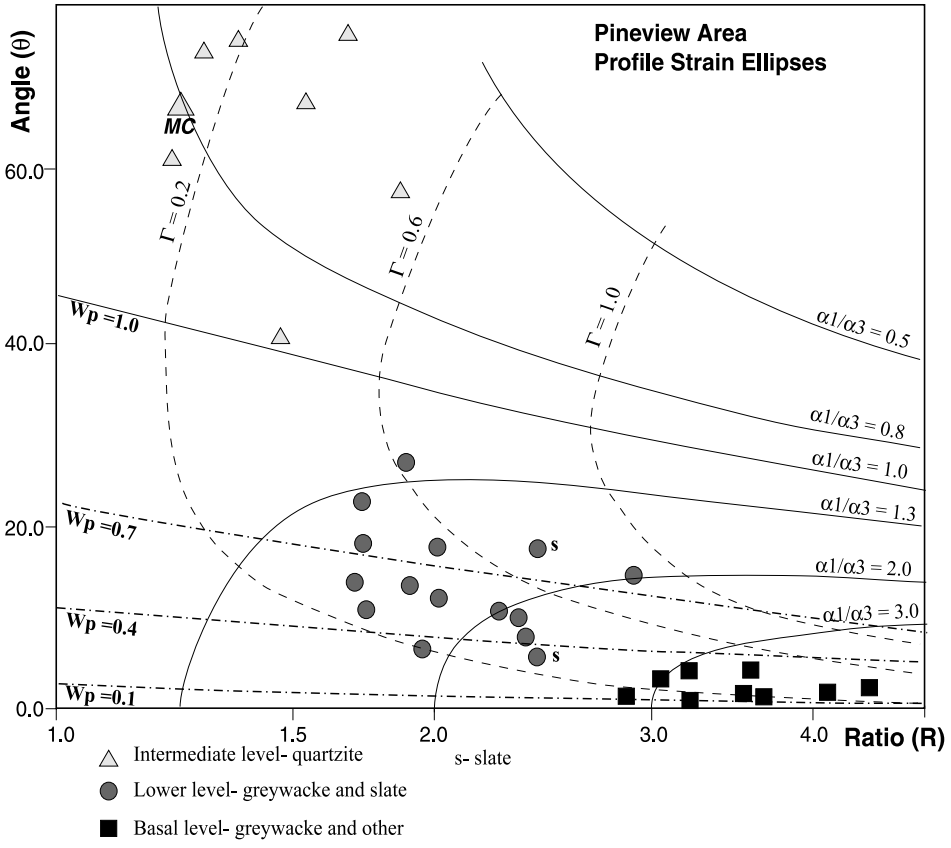

Fig. 16. Plot of strain ratio, R, and angle, θ, between ellipse long axis and bedding in profile plane for samples from the Pineview area. See Fig. 11 for explanation of contours. Intermediate-level quartzite samples have relatively low ratios and high angles, consistent with minor thrust-parallel shortening ($\alpha_1/\alpha_3 < 1$). Lower to basal level greywacke and slate samples have moderate to high ratios and moderate to very low angles, consistent with thrust-perpendicular thinning ($\alpha_1/\alpha_3 > 1$). Samples from folded areas or with significant longitudinal shear not plotted. s—slate sample. MC—average strain ratio for quartzite of Maple Canyon Formation in more western parts of the Willard sheet.

shear was low for most samples. Estimated kinematic vorticity (W) averaged about 0.4–0.6 at basal to lower levels (Table 2), slightly lower than in the Fremont Island area. Minor folds in the area produced less than 5% thrust-parallel shortening, and bed-parallel shear surfaces produced additional thrust-parallel shear.

7. Discussion

7.1. Summary of results for Willard thrust sheet study areas

Results of strain analysis for the Fremont Island and Pineview areas in the western and central parts of the Willard sheet illustrate general kinematic patterns The western part of the sheet has mostly NNE-trending minor folds and cleavage, and top-to-ESE slip lineations, whereas the central part has mostly NNW-trending minor folds and cleavage, and top-to-ENE slip lineations oblique to the overall ESE transport direction, indicating partial decoupling of early internal deformation from later large-scale transport. Shortening (Z) directions are subparallel to cleavage poles, and show systematic changes in orientation related to an overall asymptotic pattern of cleavage. X directions trend parallel, to locally acute to cleavage dip in areas with longitudinal shear. Principal axial ratios have $R_{YZ} > R_{XY}$, but microfabrics indicate only minor extension to rare shortening in Y, consistent with average volume losses of about 10–40%. Ratios, R, and angles, θ, of strain ellipses in the profile plane vary systematically with lithology and structural position. At basal levels, strongly deformed rocks have R of 3–5 and $\theta < 10°$. At lower levels, micaceous strata have R of 1.5–3 and θ from 10 to 35°, with an overall correlation between increasing ratio, decreasing angle, and increasing mica content. Overlying micaceous quartzite has R of 1.3–2 and $\theta > 50°$. These strain patterns likely record sub-simple shear with thrust-perpendicular (vertical) thinning at lower levels, thrust-parallel shear that increases overall downward and in mica-richer strata, minor thrust-parallel extension to shortening, minor longitudinal extension, and minor longitudinal shear (mostly dextral).

7.2. Kinematic models

Idealized 2-D kinematic models for a layered thrust sheet are now compared with general strain patterns for lower to

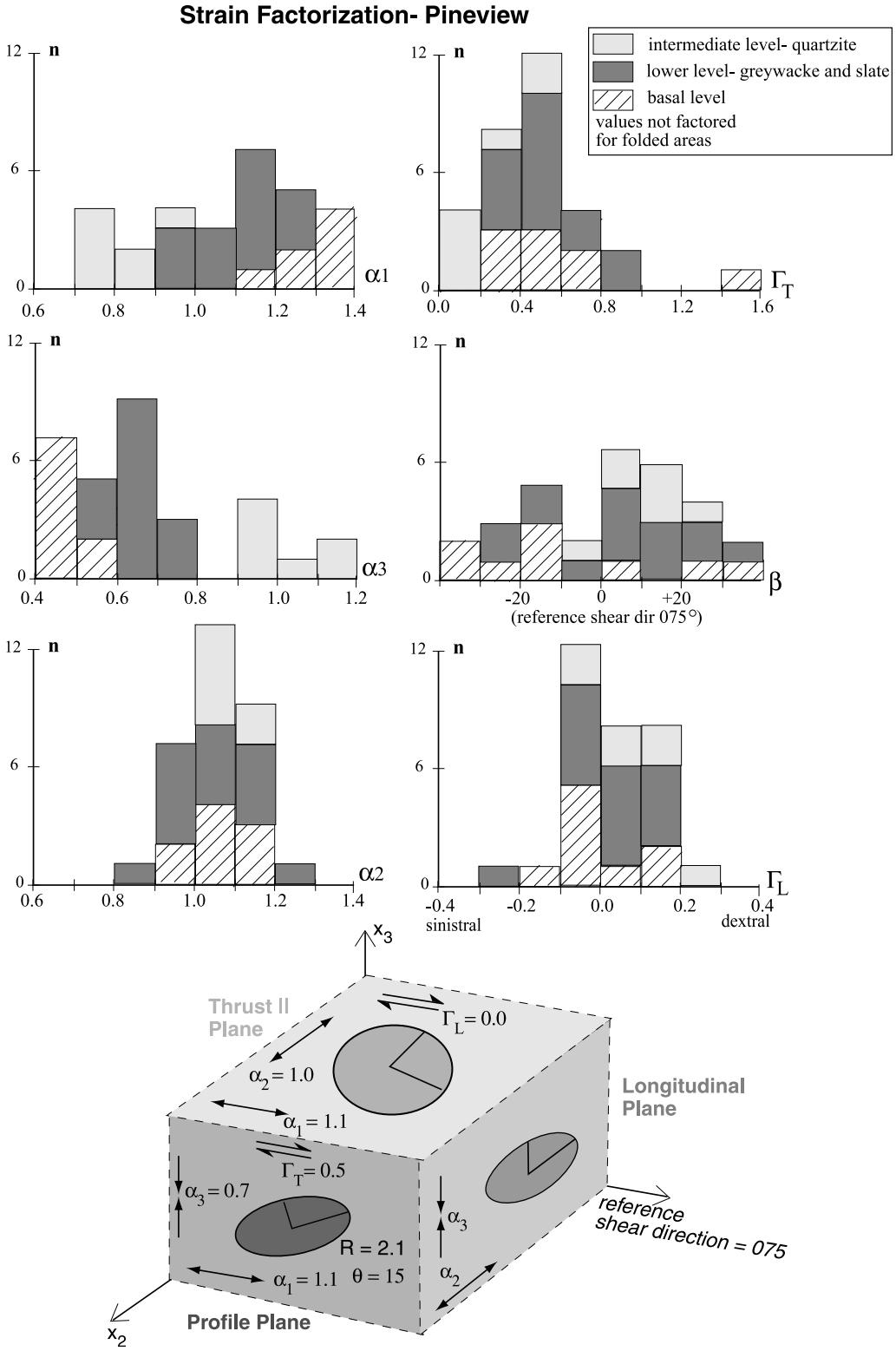

Fig. 17. Strain factorization for Pineview area. Histograms show numbers of intermediate-level quartzite (light gray), lower-level greywacke and slate (dark gray) and basal-level samples (diagonal ruled) with various ranges of thrust-parallel stretch (α_1), thrust-perpendicular stretch (α_3), longitudinal stretch (α_2), thrust-parallel shear (Γ_T), angle between reference and sample maximum shear direction (β), and longitudinal shear (Γ_L). Block diagram shows average values of strain components and section ellipses for lower level greywacke. Samples from folded areas not included. See Fig. 7A for explanation of components.

basal levels of the Willard sheet (Fig. 18). Models include: (1) heterogeneous simple shear; (2) vertical thinning with volume loss; (3) vertical thinning with thrust-parallel extension, plus discrete slip (*A*) or induced shear (*B*); and (4) a combination of these end members.

Heterogeneous simple shear that increases toward the base of the sheet (model 1) produces only limited rotation of stretching (*X*) directions with increasing strain, inconsistent with observed R–θ patterns in the Willard sheet. For example, to produce $\theta < 10°$ (typical of the basal level) by simple shear requires $R > 30$ (compared with observed ratios of 3–5). Simple shear is relatively inefficient at accumulating strain compared with pure shear, such that unreasonably high strain intensities are required to produce cleavage subparallel to thrusts by simple shear alone.

Vertical thinning with volume loss that increases downward (model 2) results in thrust-parallel cleavage ($\theta = 0°$), inconsistent with the observed asymptotic pattern of cleavage. Also, unreasonably large volume losses $>67\%$ would be required to produce observed strain ratios >3 at basal levels.

Vertical thinning with thrust-parallel extension (for constant volume, plane strain) that increases downward (model 3) produces significantly different patterns. The vertical gradient in extension requires either discrete slip along thrust-parallel surfaces that separate differently stretched layers (model 3A), or induced shear to maintain compatibility (model 3B). Model 3A results in thrust-parallel cleavage ($\theta = 0°$), inconsistent with observations. Model 3B results in a roughly asymptotic pattern of cleavage with moderate increases in R and significant decreases in θ toward the thrust, broadly consistent with patterns in the Willard sheet. Note, extension and induced shear may add a significant component of displacement to upper levels of a thrust sheet. This model can be compared to a cream cake that collapses and extrudes its weak layer as an extending shear zone, with the upper part of the cake sliding off above the cream layer. The model also results in increased shear strain and R toward the rear of the sheet, which become substantial unless vertical gradients in extension are very small. However, estimated shear for the Willard sheet increases only slightly to the west.

A combination of end members incorporating vertical thinning, volume loss, minor thrust-parallel extension, simple shear, and discrete slip (model 4), matches overall strain patterns in the Willard sheet. In this model, vertical thinning is accompanied by volume loss (or longitudinal extension), with only a small vertical gradient in thrust-parallel extension. The model also includes heterogeneous simple shear (increasing from 0.4 to 0.6 downward), and shear induced by vertical gradients in extension (increasing from 0 to 0.2 toward the back of the sheet), consistent with overall moderate shear that increases slightly westward.

Curved thrust sheets (salients) with variations in translation magnitude and direction display more complex 3-D strain patterns (Hindle and Burkhard, 1999). A simple 3-D kinematic model that incorporates longitudinal extension and longitudinal (wrench) shear, which are minor but widespread components in the Willard sheet, is shown in Fig. 19. The Paris–Meade–Willard system defines a salient convex to the east that has a longitudinal gradient in bulk translation magnitude and direction, from about 60 km toward 090° in the central part, to 50 km of slip toward 105° in the southern part over a distance of about 120 km (Fig. 2A). A 10 km change in displacement over a 120 km distance yields an average dextral shear of about 0.1, similar to values in much of the southern Willard sheet. A 15° change in translation direction over the area results in an average longitudinal extension of about 0.1, again similar to values in much of the southern Willard sheet. The change in translation magnitude and direction partly reflect isopach patterns that are also convex to the east for most strata, such that the sedimentary wedge thickens and shortening increases northward toward the central part of the salient. Local sinistral shear in the Pineview area, however, may reflect locally increased shortening along the margin of the Oquirrh Basin that thickens southwestward, oblique to other isopach patterns.

7.3. Comparison with other thrust sheets

Strain patterns in the Willard thrust sheet record sub-simple shear and display broad similarities to other thrust sheets, as briefly discussed below and illustrated in Fig. 20. Greywacke deformed at low metamorphic grades ($T \sim 300$ °C) near the Glarus thrust has moderate strain ($R \sim 1.5$–2) and thrust-subparallel cleavage ($\theta < 10°$), reflecting thrust-perpendicular (vertical) thinning, significant volume loss ($>30\%$), limited thrust-parallel stretching, and minor thrust-parallel shear, possibly due to the presence of a very weak fault zone that did not transmit significant shear traction (Ring et al., 2001), broadly similar to patterns for micaceous strata in the Willard sheet. Some accretionary wedges also contain low-grade micaceous rocks that experienced significant vertical thinning and volume loss (e.g. Freehan and Brandon, 1999). Quartzite deformed at low grades in the Moine thrust zone generally has moderate strain ($R \sim 1.5$–2) and steep cleavage ($\theta > 45°$), reflecting thrust-parallel shortening and minor thrust-parallel shear (Coward and Kim, 1981), with some areas also experiencing minor wrench shear and longitudinal extension (Coward and Potts, 1983), broadly similar to patterns of micaceous to arkosic quartzite in the Willard sheet. Localized mylonite zones adjacent to the Moine thrust, however, have much higher strain ($R \sim 50$) and low-angle cleavage ($\theta < 2°$), recording concentrated thrust-parallel extension and shear (Sanderson, 1982), partly similar to higher strained rocks at the base of the Willard sheet, although strain could not be measured for the fault core. For comparison, limestone deformed at medium grade ($T \sim 400$ °C) in the Northern Appenines has widespread high strain ($R \sim 5$–10) and cleavage at low angles to bedding ($\theta < 10°$), reflecting

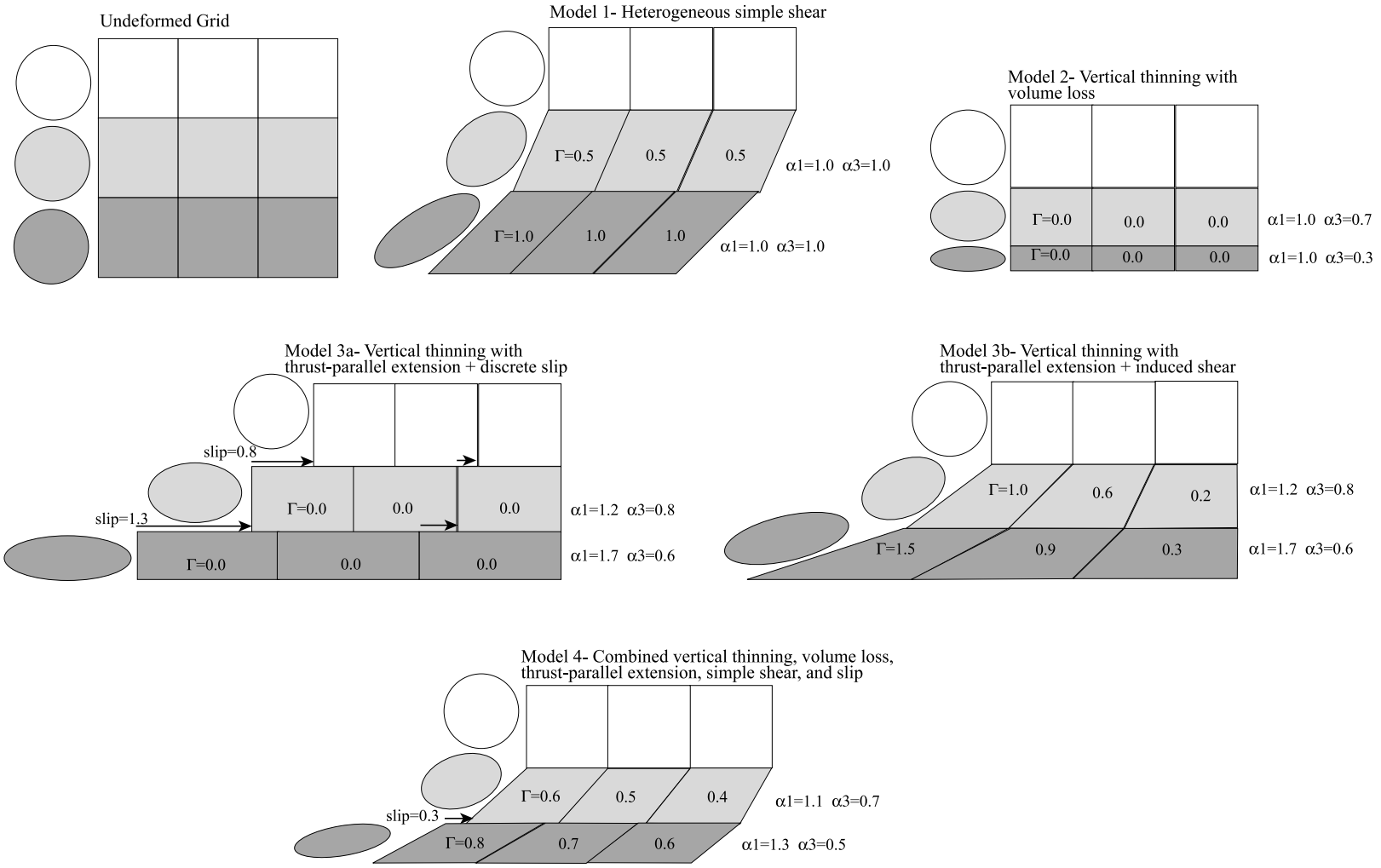

Fig. 18. Two-dimensional kinematic models, with deformed grids with strain ellipses and values of thrust-parallel shear (Γ), and thrust-parallel and -perpendicular stretch (α_1 and α_3) indicated. End-member models are: 1—heterogeneous thrust-parallel shear, 2—vertical thinning with volume loss, and 3—vertical thinning with thrust-parallel extension plus either discrete slip (A) or induced shear (B). These models are inconsistent with observed strain patterns in the Willard sheet. Combined model (4) with vertical thinning, volume loss, minor thrust-parallel extension, thrust-parallel shear, and discrete slip matches general patterns in the Willard sheet.

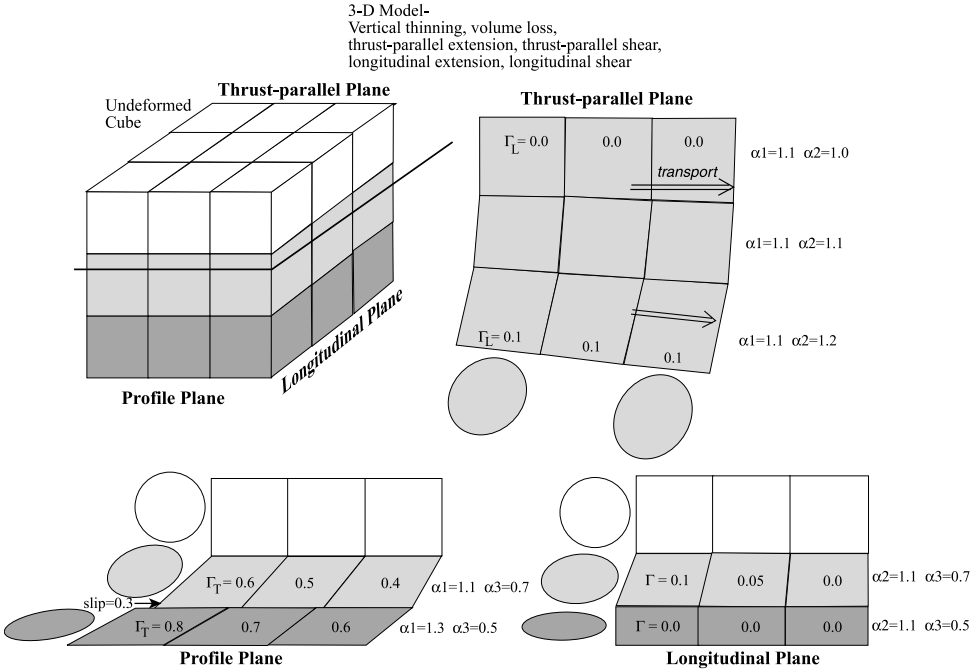

Fig. 19. Three-dimensional kinematic model shows grids and strain ellipses for profile, longitudinal, and thrust-parallel planes. Values of shear and stretches in each plane are indicated. Note minor longitudinal extension (α_2) and longitudinal shear (Γ_L) related to changes in translation in thrust-parallel plane.

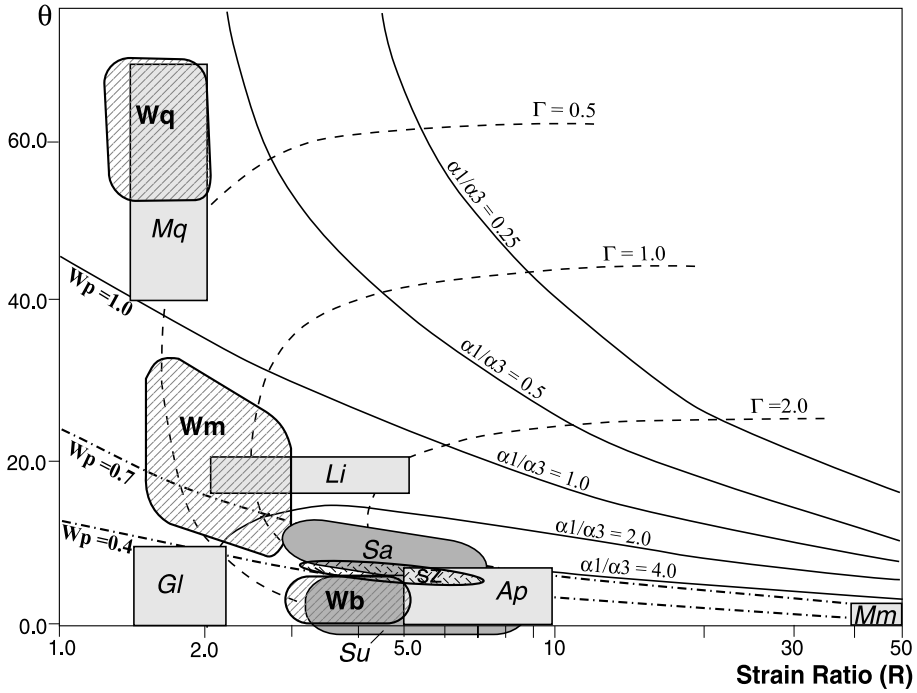

Fig. 20. Plot of strain ratios, R, and angles, θ, for various thrust sheets and shear zones. Typical values for the Willard thrust sheet (diagonally ruled patterns) are: Wq—micaceous to arkosic quartzite at intermediate levels, Wm—micaceous strata at lower levels, and Wb—basal levels. Typical values for other thrust sheets (light gray) are: Mq—Moine quartzite (Coward and Kim, 1981); Mm—Moine mylonite zones (Sanderson, 1982); Gl—Glarus greywacke (Ring et al., 2001); Ap—Northern Appenine limestone (Kligfield et al., 1981); and Li—Ligurian Alps meta-conglomerate (Seno et al., 1998). Values for transpressive belts (medium gray) are: Su—Superior Province belt (Czeck and Hudleston, 2003); and Sa—Sambagawa belt (Wallis, 1995). Example values for shear zones (stippled pattern) are labeled SZ (Eyster and Bailey, 2001). Contours of thrust-parallel shear (Γ), ratio of thrust-parallel to thrust-perpendicular stretch (α_1/α_3), and mean kinematic vorticity for plane strain (W_P) indicated. Results for all examples indicate importance of sub-simple shear.

widespread vertical thinning, thrust-parallel shear, volume loss, and thrust-parallel extension (Kligfield et al., 1981). Meta-conglomerate deformed at medium grade in the Ligurian Alps also has widespread high strain ($R \sim 2$–5) and low angle cleavage ($\theta \sim 20°$), consistent with thrust-parallel shear and vertical thinning (Seno et al., 1998).

Interestingly, a variety of transpressional belts and shear zones have also experienced sub-simple shear (Fig. 20). A transpressive belt in the Superior Province containing deformed conglomerates has high strain ($R \sim 3$–9) and cleavage at low angles to the belt boundary ($\theta < 10°$), recording components of belt-normal shortening, simple shear, and vertical to horizontal extrusion (Czeck and Hudleston, 2003). The Sambagawa belt of Japan has broadly similar strain patterns, and porphyroclast relations, quartz c-axis fabrics, and vein geometries indicate relatively low kinematic vorticity ($W \sim 0.4$–0.7) (Wallis, 1995). Shear zones studied by Eyster and Bailey (2001) also have relatively high strains ($R \sim 3$–8), cleavage at low angles to zone boundaries ($\theta \sim 10°$), and low kinematic vorticity ($W \sim 0.3$–0.4).

All of the thrust sheets, transpressive belts, and shear zones discussed here underwent sub-simple shear, which may reflect common mechanical processes. The presence of weak micaceous layers, fault zones at elevated fluid pressure, and strain softening may lead to concentrated deformation in thrust sheets (Gilotti, 1989; Gray, 1995), and shear zones (Mitra, 1978). Bedding above flats tends to remain parallel to thrusts during deformation, such that deformation and rheologic properties of thrust sheets are banded (Sanderson, 1982). Strain partitioning may be important, with simple shear concentrated in weaker layers (e.g. slate), and greater pure shear in stronger layers (e.g. quartzite), similar to patterns of some shear zones and intervening wall-rock lozenges (Goodwin and Williams, 1996). Thrust sheets also display three-dimensional complications from oblique ramps, lateral changes in weak layers, and varying slip directions in salients (Coward and Potts, 1983; Hindle and Burkhard, 1999), just as shear zones display complications from bends, changes in thickness, and variations in shear directions (Coward, 1976; Hudleston, 1999).

Varying strain patterns between thrust sheets may reflect different environmental factors (temperature and fluid pressure), lithologies, and boundary conditions. Unmetamorphosed, external thrust sheets typically have only limited thrust-parallel shortening and minor simple shear concentrated at bases of sheets and along weak horizons (Wojtal, 1986; Mitra, 1994). Thrust sheets deformed at low metamorphic grades include stronger quartz-rich strata with thrust-parallel shortening, and weaker micaceous strata with shear and thrust-perpendicular thinning (Fig. 20). In detail, thrust sheets vary from having broad zones of distributed strain where thick intervals of weak rock are present (Gray, 1995), to having narrow zones of strain concentrated near faults where thick intervals of strong rock are present (Mitra and Boyer, 1999). Thrust sheets deformed at medium grade tend to have higher and more uniform strains that include components of thrust-perpendicular thinning (Fig. 20). In general, the presence of micaceous layers, downward increases in temperature, and softening along fault zones produces weak intervals and effective anisotropy. Far-field stress inclined to layering may rotate into being subperpendicular to weak intervals that cannot transmit significant shear traction, resulting in significant components of pure shear, and stretching fault zones (Means, 1989).

8. Conclusions

Microtextures, mesoscopic structures, and finite strain patterns change systematically with structural position and lithology in the Willard sheet. The sheet contains: (1) a high-strain, basal level above a fault core of mylonite and ultracataclasite; (2) a medium-strain, lower level with abundant mica-rich slate, diamictite, and greywacke; and (3) a lower-strain, intermediate level with abundant micaceous to arkosic quartzite. Typical strain ratios, R, and angles, θ, in the profile plane vary from 3 to 5 and $< 10°$ at basal levels, 1.5–3 and 10–35° at lower levels, and 1.3–2 and $> 50°$ at intermediate levels, with overall correlations between increasing R, decreasing θ, decreasing distance to thrust, and increasing mica content. These strain values reflect sub-simple shear with thrust-perpendicular thinning, volume loss, and thrust-parallel shear that increase downward and in weaker layers, and minor thrust-parallel shortening to extension. Although plane strain provides a reasonable approximation for some samples, widespread minor longitudinal extension and wrench shear add three-dimensional complexities. These kinematic patterns reflect rheological layering of the thrust sheet, which includes a very weak basal fault zone, a weak mica-rich lower level deformed by crystal plasticity and mass transfer processes at $T = 300$–400 °C, and a higher-strength upper part deformed at lower temperatures.

Acknowledgements

This manuscript benefited significantly from constructive reviews and thoughtful suggestions by Dyanna Czeck and Peter Hudleston. Parts of this research were supported by NSF grant EAR-9219809 and the Weber State University Endowed Scholar Program.

Appendix A

Three-dimensional finite strain values were factored into strain components, assuming steady state paths with simultaneous pure and simple shear, using the following relations. The velocity gradient matrix, L, for a local

reference frame with the x_1–x_2 plane parallel to a thrust (and bedding) (Fig. 7A), is given by:

$$\mathbf{L} = \begin{bmatrix} \dot{\alpha}_{11} & \dot{\gamma}_{12} & \dot{\gamma}_{13} \\ 0 & \dot{\alpha}_{22} & \dot{\gamma}_{23} \\ 0 & 0 & \dot{\alpha}_{33} \end{bmatrix} \tag{A1}$$

Following Tikoff and Fossen (1995), a normalized time, $t' = 1$, can be defined for steady state paths to give corresponding coaxial stretch (α) and shear (Γ) strain components:

$$\alpha_i = \exp(\dot{\alpha}_{ii}) \quad \text{and} \quad \Gamma_{jk} = \dot{\gamma}_{jk} \tag{A2}$$

Using these components, the deformation gradient matrix, D, in the local reference frame is:

$$\mathbf{D} = \begin{bmatrix} \alpha_1 & \Gamma_{12}(\alpha_1 - \alpha_2)/\ln(\alpha_1/\alpha_2) & \Gamma_{13}(\alpha_1 - \alpha_3)/\ln(\alpha_1/\alpha_3) + \text{term} \\ 0 & \alpha_2 & \Gamma_{23}(\alpha_2 - \alpha_3)/\ln(\alpha_2/\alpha_3) \\ 0 & 0 & \alpha_3 \end{bmatrix} \tag{A3}$$

The cross-term is not written out for simplicity (see Tikoff and Fossen (1995) for complete equation). The Finger tensor, F, in the local reference frame is then given by:

$$\mathbf{F} = \mathbf{D}^{\mathrm{T}}\mathbf{D} \tag{A4}$$

F is also given by:

$$\mathbf{F} = \mathbf{R}^{\mathrm{T}}\mathbf{Q}R \tag{A5}$$

where Q is the matrix representation of the three-dimensional strain ellipsoid in a N–E-vertical reference frame, and R is the rotation matrix for the local reference frame. Thus, elements of F can be calculated from Q using Eq. (A5), elements of D can be calculated from F using Eq. (A4), and elements of L and strain components can be calculated from D using Eqs. (A2) and (A3). Ratios, R, and angles, θ, of section ellipses along planes in the local reference frame can also be calculated from F. Note, scaling Q for volume change, Δv, affects diagonal terms of L by the relation:

$$\dot{\alpha}_{ii} = \dot{\alpha}^{v}_{ii} + \ln(1 + \Delta v)/3 \tag{A6}$$

where $\dot{\alpha}^{v}_{ii}$is the stretch rate for corresponding isovolumetric deformation. L can be split into symmetric (strain rate), antisymmetric (internal rotation rate), and volume change parts by:

$$\mathrm{L} = \begin{bmatrix} \dot{\alpha}_{11} & \dot{\gamma}_{12}/2 & \dot{\gamma}_{13}/2 \\ \dot{\gamma}_{12}/2 & \dot{\alpha}_{22} & \dot{\gamma}_{23}/2 \\ \dot{\gamma}_{13}/2 & \dot{\gamma}_{23}/2 & \dot{\alpha}_{33} \end{bmatrix} + \begin{bmatrix} 0 & \dot{\gamma}_{12}/2 & \dot{\gamma}_{13}/2 \\ -\dot{\gamma}_{12}/2 & 0 & \dot{\gamma}_{23}/2 \\ -\dot{\gamma}_{13}/2 & -\dot{\gamma}_{23}/2 & 0 \end{bmatrix} + \ln(1 + \Delta v)/3\mathbf{I} \tag{A7}$$

where I is the identity matrix. The mean kinematic vorticity number, W, is then given by:

$$W = \frac{\left(\dot{\gamma}_{12}^2 + \dot{\gamma}_{13}^2 + \dot{\gamma}_{23}^2\right)^{1/2}}{\left(2\left[\left(\dot{\alpha}^{v}_{11}\right)^2 + \left(\dot{\alpha}^{v}_{22}\right)^2 + \left(\dot{\alpha}^{v}_{33}\right)^2\right] + \dot{\gamma}_{12}^2 + \dot{\gamma}_{13}^2 + \dot{\gamma}_{23}^2\right)^{1/2}} \tag{A8}$$

References

Barr, M., Coward, M.P., 1974. A method for the measurement of volume change. Geological Magazine 111, 293–296.

Boyer, S.E., Elliot, D., 1982. Thrust systems. American Association Petroleum Geologists Bulletin 66, 1196–1230.

Coogan, J.C., 1992. Thrust systems and displacement transfer in the Wyoming–Idaho–Utah thrust belt. PhD dissertation, University of Wyoming, 240pp.

Coogan, J.C., King, J.K., 1998. Geologic map of the Ogden 30′×60′ quadrangle. Utah Geological Survey Open File Report 365, scale 1:100,000.

Coward, M.P., 1976. Strain within ductile shear zones. Tectonophysics 34, 181–197.

Coward, M.P., Kim, J.H., 1981. Strain within thrust sheets, in: McClay, K.R., Price, N.J. (Eds.), Thrust and Nappe Tectonics Special Publications of the Geological Society of London, 9, pp. 275–292.

Coward, M.P., Potts, G.J., 1983. Complex strain patterns developed at the frontal and lateral tips to shear zones and thrust zones. Journal of Structural Geology 5, 383–399.

Crittenden Jr., M.D., 1972. Willard thrust and Cache allochthon, Utah. Geological Society of America Bulletin 83, 2871–2880.

Czeck, D.M., Hudleston, J., 2003. Testing models for obliquely plunging lineations in transpression: a natural example and theoretical discussion. Journal of Structural Geology 25, 959–982.

DeCelles, G., Pile, H.T., Coogan, J.C., 1993. Kinematic history of the Meade thrust based on provenance of the Bechler Conglomerate at Red Mountain, Idaho, Sevier thrust belt. Tectonics 12, 1436–1450.

Erslev, E.A., 1988. Normalized center-to-center strain analysis of packed aggregates. Journal of Structural Geology 10, 201–209.

Evans, J.P., Neves, D.S., 1992. Footwall deformation along the Willard thrust Sevier orogenic belt: implications for mechanisms, timing, and kinematics. Geological Society of America Bulletin 104, 516–527.

Eyster, E.L., Bailey, C.M., 2001. Vorticity analysis of extensional and transpressional high-strain zones; examples from the Arizona Basin and Range and Virginia Piedmont. Geological Society of America Abstracts with Programs 33 (2), 5.

Freehan, J.G., Brandon, M.T., 1999. Contribution of ductile flow to exhumation of low T–high P metamorphic rocks: San Juan–Cascade nappes, NW Washington State. Journal of Geophysical Research 104, 10883–10901.

Gilotti, J.A., 1989. Reaction progress during mylonitization of basaltic dikes along the Sarv thrust. Contributions to Mineralogy and Petrology 101, 30–45.

Goodwin, L.B., Williams, F., 1996. Deformation path partitioning within a transpressive shear zone, Marble Cove, Newfoundland. Journal of Structural Geology 18, 975–990.

Gray, D.R., 1995. Thrust kinematics and transposition fabrics from a basal detachment zone, eastern Australia. Journal of Structural Geology 17, 1637–1654.

Hindle, D., Burkhard, M., 1999. Strain, displacement and rotation associated with the formation of curvature in fold belts; the example of the Jura arc. Journal of Structural Geology 21, 1089–1101.

Hintze, L., 1981. Geologic map of Utah. Utah Geological Survey, scale 1:500,000.

Hossack, J.R., 1968. Pebble deformation and thrusting in the Bygdin area (Southern Norway). Tectonophysics 5, 315–339.

Hudleston, P., 1999. Strain compatibility and shear zones: is there a problem?. Journal of Structural Geology 21, 923–932.

Ismat, Z., Mitra, G., 2001. Folding by cataclastic flow at shallow crustal levels in the Canyon Range, Sevier orogenic belt, west-central Utah. Journal of Structural Geology 23, 355–378.

Kligfield, R., Carmignani, L., Owens, W.H., 1981. Strain analysis of a Northern Apennine shear zone using deformed marble breccias. Journal of Structural Geology 3, 421–436.

Lisle, R.J., 1985. Geometrical Strain Analysis, a Manual for the R_f–ϕ Technique. Pergamon Press, Oxford. 99pp.

McNaught, M., 1994. Modifying the normalized Fry method for aggregates of non-elliptical grains. Journal of Structural Geology 16, 493–503.

McNeil, M.A., Smith, R.B., 1992. Upper crustal structure of the northern Wasatch Front, Utah, from seismic reflection and gravity data. Utah Geological Survey Contract Report 92-7, 62pp.

Means, W.D., 1989. Stretching faults. Geology 17, 893–896.

Mitra, G., 1978. Ductile deformation zones and mylonites: the mechanical processes involved in the deformation of crystalline basement rocks. American Journal of Science 278, 1057–1084.

Mitra, G., 1994. Strain variation in thrust sheets across the Sevier fold-and-thrust belt (Idaho–Utah–Wyoming): implications for section restoration and wedge taper evolution. Journal of Structural Geology 16, 585–602.

Mitra, G., Boyer, S.E., 1999. Strain in the Lewis thrust sheet, NW Montana fold-and-thrust belt: implications for basin restoration and estimates of critical taper. Geological Society of America Abstracts with Programs 31, 237.

Mukul, M., Mitra, G., 1998. Finite strain and strain variation analysis in the Sheeprock thrust sheet: an internal thrust sheet in the Provo salient of the Sevier fold-and-thrust belt, Central Utah. Journal of Structural Geology 20, 385–405.

Onasch, C.M., 1984. Application of the R_f–ϕ technique to elliptical markers deformed by pressure solution. Tectonophysics 110, 157–165.

Owens, W.H., 1984. The calculation of a best-fit ellipsoid from elliptical sections on arbitrarily oriented planes. Journal of Structural Geology 6, 571–578.

Peach, C.J., Lisle, R.J., 1979. A Fortran IV program for the analysis of tectonic strain using deformed elliptical markers. Computers and Geosciences 5, 325–344.

Ramsay, J.G., Casey, M., Kligfield, R., 1983. Role of shear in development of the Helvetic fold–thrust belt of Switzerland. Geology 11, 439–442.

Ridley, J., 1986. Parallel stretching lineations and fold axes oblique to a shear displacement direction—a model and observations. Journal of Structural Geology 8, 647–653.

Ring, U., Brandon, M.T., Ramthun, A., 2001. Solution-mass-transfer deformation adjacent to the Glarus thrust, with implications for the tectonic evolution of the Alpine wedge in eastern Switzerland. Journal of Structural Geology 23, 1491–1505.

Royse Jr., F., 1993. An overview of the geologic structure of the thrust belt in Wyoming, northern Utah, and eastern Idaho, in: Snoke, A.W., Steidtmann, J.R., Roberts, S.M. (Eds.), Geology of Wyoming Geological Survey of Wyoming Memoir, 5, pp. 272–311.

Sanderson, D.J., 1982. Models of strain variation in nappes and thrust sheets: a review. Tectonophysics 88, 201–233.

Seno, S., Dallagiovanna, G., Vanossi, M., 1998. From finite strain data to strain history: a model for a sector of the Ligurian Alps, Italy. Journal of Structural Geology 20, 573–585.

Shimamoto, T., Ikeda, Y., 1976. A simple algebraic method for strain estimation from deformed ellipsoidal objects—basic theory. Tectonophysics 36, 315–337.

Simpson, C., De Paor, D.G., 1993. Strain and kinematic analysis in general shear zones. Journal of Structural Geology 15, 1–20.

Tikoff, B., Fossen, H., 1993. Simultaneous pure and simple shear: the unifying deformation matrix. Tectonophysics 217, 267–283.

Tikoff, B., Fossen, H., 1995. The limitations of three-dimensional kinematic vorticity analysis. Journal of Structural Geology 17, 1771–1784.

Treagus, S.H., Treagus, J.E., 2002. Studies of strain and rheology of conglomerates. Journal of Structural Geology 24, 1541–1567.

Wallis, S., 1995. Vorticity analysis and recognition of ductile extension in the Sambagawa belt, SW Japan. Journal of Structural Geology 17, 1077–1093.

Wojtal, S., 1986. Deformation within foreland thrust sheets by populations of minor faults. Journal of Structural Geology 8, 341–360.

Yonkee, W.A., 1992. Basement-cover relations, Sevier orogenic belt, northern Utah. Geological Society of America Bulletin 104, 280–302.

Yonkee, W.A., 1997. Kinematics and mechanics of the Willard thrust sheet, central part of the Sevier orogenic wedge, north-central Utah. Brigham Young University Studies 42, 341–354.

Yonkee, W.A., Parry, W.T., Bruhn, R.L., Cashman, C., 1989. Thermal models of thrust faulting: constraints from fluid inclusion observations, Willard thrust sheet, Idaho–Utah–Wyoming thrust belt. Geological Society of America Bulletin 101, 304–313.